Pore structure characteristics and their influencing factors: A case study from the middle jurassic mixed siliciclastic carbonate rocks, Turpan-Hami basin, Northwest China

Tianjun Li [a,b], Zhilong Huang [a,b,*], Jing Zhao [a], Xiongfei Xu [c], Xiaobo Guo [d]

[a] State Key Laboratory of Petroleum Resources and Prospecting, China University of Petroleum (Beijing), Beijng, 102249, China
[b] College of Geosciences, China University of Petroleum (Beijing), Beijng, 102249, China
[c] PetroChina Tuha Oilfield Company, Hami, 839009, China
[d] Xi'an Shiyou University, Xi'an, 710065, China

ARTICLE INFO

ABSTRACT

The mixed siliciclastic-carbonate rocks of the second member of the Qiketai Formation (J_2q_2) in the Turpan-Hami Basin are lacustrine tight oil reservoir with vitrinite reflectance values (%, Ro) ranging from 0.64% to 0.81%. X-ray diffraction (XRD), thin sections, field emission scanning electron microscopy (FE-SEM) of argon-milled thin sections, low-temperature N_2 adsorption (LNTA), and nuclear magnetic resonance (NMR) analyses were performed to investigate the pore structure characteristics and their influencing factors of the mixed siliciclastic-carbonate reservoirs. The results show that the tight reservoir has a medium-high total organic carbon (TOC) content, and the sedimentary textures include laminated, massive, and intraclasts-rich types. Nanometer scale interparticle pores and microfractures are dominant in the tight reservoirs. The small pores (2–100 nm) make a dominant contribution to the nanoscale storage space according to the comprehensive analysis of the T_2 spectra of NMR. Reversed S-shaped isotherms obtained from N_2 adsorption are type IV, and hysteresis loops indicate that the shape of pores include slit-or plate-like, ink-bottle-shaped and mixtures of the two. BET surface areas and BJH total pore volume vary from 1.707 m^2/g to 8.556 m^2/g and 1.13 cm^3/100 g to 3.0 cm^3/100 g, with an average of 4.31 m^2/g and 1.848 cm^3/100 g, respectively. The massive and intraclasts-rich rocks have higher NMR porosities, pore sizes and pore volumes than the laminated rocks. Based on the Frenkel-Halsey-Hill model of low-temperature N_2 adsorption, the fractal dimensions D_1 and D_2 are 2.4305–2.7081 and 2.2667–2.6070, respectively. The correlations between the pore structure parameters and the mineralogical composition, TOC content, and fractal dimension reveal that dolomite makes greater contribution to the pore volume and movable fluid saturation than the siliciclastic gains and organic matter, resulting in higher fractal dimensions and more complicated pore structure. In addition, the clay minerals increase pore specific surface area and its complexity in the tight reservoirs. The samples with high silicate mineral and TOC contents tend to contain lower specific surface areas and pore volumes, resulting in lower fractal dimensions and more simplistic pore structure than clay rich samples. Therefore, the complex mineralogical composition, various sedimentary textures and organic matter content all play important roles in the development of pore network.

1. Introduction

Mixed siliciclastic-carbonate rocks are an important type of continental tight oil reservoir (Zou et al., 2015; Hu et al., 2018). Compared with shale and tight carbonate rocks, mixed siliciclastic-carbonate rocks are characterized by a complex lithology and various sedimentary textures and mineralogical compositions (Zhu et al., 2019a; Li et al., 2020).

According to a recent evaluation of Ministry of Land and Resources, the geological resources of tight oil in China's nine key basins are about 14.66 billion tons. Their technically recoverable resources are 1.454 billion tons, among which the proportion of the geological resources of mixed siliciclastic-carbonate rock tight oil is more than 40% (Zou et al., 2015; Li et al., 2017), which its technically recoverable part is294 million tons, making up more than 20% (Zhu et al., 2019a). The huge

---

resource potential makes some scholars interest in the studies of mixed siliciclastic-carbonate rock, especially in terms of classification, nomenclature, sedimentary environment, and reservoir heterogeneity (Coffey et al., 2004; Feng et al., 2011; Komatsu et al., 2014). Until now, the genetic types and sedimentary environment of mixed siliciclastic-carbonate rocks have been studied for more than 50 years, and previous scholars have reported numerous breakthroughs achievements (Mount et al., 1984; Tcherepanov et al., 2008; Ye et al., 2019; Xu et al., 2019). However, understanding of the reservoir characteristics of these rocks is relatively lacking, particularly in terms of their pore structures and key controlling factors (Zhang et al., 2018; Li et al., 2020). Therefore, it is urgent to make clear the pore structure of the widely distributed mixed siliciclastic-carbonate rocks in the continental basins of China (Feng et al., 2011; Ye et al., 2018; Li et al., 2020).

Mixed siliciclastic-carbonate tight reservoirs are generally characterized as a heterogeneous porous material with a complex pore structure and pore sizes ranging from nanometers to micrometers (Li et al., 2020). The variability of pore structure is the main factor influencing the reservoir and flow ability of tight reservoirs (Yang et al., 2017a, 2017b; Zhu et al., 2019b). Many pore structures and their influencing factors have been investigated in studies of marine over-mature and lacustrine medium-high maturity shales. The results of these studies suggest that TOC content and mineralogical composition have important effects on the pore structure parameters including pore size distribution, movable fluid content, total pore volume (TPV), and specific surface area (SSA) (Chalmers et al., 2012; Yang et al., 2014). The TOC content is generally positively correlated with SSA and TPV, and the quartz content also has a positive correlation with SSA and TPV in high-over mature marine shale (Clarkson et al., 2013). However, for lacustrine shales, the TOC, silicate and clay mineral contents have complex relationships with the pore structure parameters (e.g., TPV and SSA; Liu et al., 2015; Li et al., 2017). For example, the Qingshankou lacustrine mature shale in the Songliao Basin, the relationship between the TOC and the pore structure parameters exhibits a bell shaped curve, with maximum values at 2.5–3 wt.% TOC. The clay mineral content is negatively correlated with the pore structure parameters, while the quartz content is not significantly correlated with the pore structure parameters (Wang et al., 2015). However, for the lacustrine shales of the Yanchang Formation in the Ordos Basin and the Shahejie Formation in the Bohai Bay Basin, the TOC and calcareous contents are positively correlated with the pore structure parameters (e.g., TPV and SSA); the quartz and clay mineral contents have weak negative correlations with the pore structure parameters (Liu et al., 2014; Jiang et al., 2016; Li et al., 2017). The above results suggest that the pore structure and its influencing factors of lacustrine shale is very complex. In contrast, few studies have been conducted on tight mixed siliciclastic-carbonate reservoirs with complex mineralogical composition and various sedimentary textures. Therefore, clearly understanding the pore structure of mixed siliciclastic-carbonate rocks is significant for evaluating their hydrocarbon fluid storage and flow mechanisms (Zhu et al., 2019b).

The characteristics of the microscopic pore structures of tight reservoirs are an important aspect of research on unconventional reservoirs. The quantitative and qualitative methods of characterizing the microscopic pore structure mainly include high resolution microscopic observations and fluid injection methods (Loucks et al., 2012; Li et al., 2019a; Liu et al., 2019a,b). Generally, the microscopic observations of pore size, connectivity, and shape are performed using field emission scanning electron microscopy (FE-SEM) and micron-CT (computerized tomography) scans (Lai et al., 2018; Saif et al., 2017). The fluid invasion technologies including the gas adsorption, nuclear magnetic resonance (NMR), and mercury intrusion methods, which can quantitatively characterize the pore volume, pore sizes, and so on. Different characterization methods are suitable for different ranges of pore sizes. Generally, N_2 adsorption is suitable for characterizing pore structures with a maximum pore size of 200 nm (Bai et al., 2014; Li et al., 2019b; Zhu et al., 2019b). NMR can investigate reservoir pore structures with a

pore size distribution range of 2 nm–10 μm (Bai et al., 2014). Therefore, it is necessary to choose an appropriate method to study the pore structure quantitatively. Recently, fractal dimension based on N_2 adsorption and NMR data has become popular for estimating the irregularity of pore structure and surfaces in shale and coal. The fractal characteristics of both marine and lacustrine shales and their impact on pore structure have been discussed (Yang et al., 2014; Liu et al., 2015; Li et al., 2019a, 2019b). Thus far, few studies have been conducted on the fractal pore characteristics of mixed siliciclastic-carbonate reservoirs. In order to better understanding of pore structure and the influence of mineralogical composition and TOC content on pore network of mixed siliciclastic-carbonate reservoirs, SEM imaging of argon-milled thin sections, low-temperature N_2 adsorption and NMR were conducted on the mixed siliciclastic-carbonate rocks in the J_2q_2. Based on these analytical experiments, the impact of the mineralogical composition and TOC content on the pore structure was discussed, and the fractal dimension obtained from the N_2 adsorption data was estimated the heterogeneity of the pore surface and structure. The results of this study provide a clear understanding of the pore structure characteristics and their influencing factors of mixed siliciclastic-carbonate rocks deposited in a mixed siliciclastic-carbonate sedimentary environments.

2. Geological background

Shengbei Sag is the largest hydrocarbon generating sag of the Turpan-Hami Basin in Northwest China, with an area of about 3000 km². Its western part is near to the Qiudong Sag, the southern part is bounded by the Huoyanshan thrust belt, and the northern part is bounded by the Bogda Piedmont belt (Xiao et al., 2013) (Fig. 1a and b). The source rocks are widely developed in the Middle Jurassic strata (Yang et al., 2006; Zhu et al., 2014), which is divided into three formations from the bottom to the top, Xishanyao Formation (J_2x), Sanjianfang Formation(J_2s) and Qiketai Formation (J_2q). The Xishanyao Formation mainly consists of coal-rich source rocks and sandstones, deposited in a marshy environment (Guo et al., 2018). The Qiketai Formation can be divided into two members (J_2q_1 and J_2q_2) from the bottom to the top (Fig. 1c). The sedimentary environment of the first member of Qiketai Formation (J_2q_1) is similar to that of the Xishanyao Formation (J_2x) and Sanjianfang Formation(J_2s), deposited in a lacustrine marshy environment (Guo et al., 2018). The Turpan-Hami Basin was in the transitional stage between a peneplain depression basin and a foreland basin during the deposition of J_2q_2, and the tectonic activity was still relatively weak, leading to moderate topography and a semi-humid to semi-arid paleoclimate climate (Li et al., 1997a, 1997b; Zhu et al., 2014). In addition, a large-scale lake transgression occurred in the early and middle stages of J_2q_2. At this time, the depocenters of the lacustrine basin were concentrated in the central and western regions of the basin, and the largest water catchment was located in the Shengbei subsag of the Taibei Sag (Li et al., 1997). There are two main types of source rocks in the Middle Jurassic, including the coal-bearing source rocks of Xishanyao Formation and the low-maturity lacustrine source rocks of J_2q_2 (Li et al., 2020).

Recently, a set of mixed siliciclastic-carbonate sedimentary rocks coexisting with the low-maturity source rocks of J_2q_2 have attracted much attention in slope-deep sag area of the Shengbei Sag. This set of mixed siliciclastic-carbonate sedimentary rocks is the most important target area of tight oil exploration in the Shengbei Sag (Feng et al., 2019). The mixed siliciclastic-carbonate rocks of the J_2q_2 Member include silt-bearing argillaceous micritic limestone, silty micritic limestone, a small number of calcitic dolomite, argillaceous dolomite and silty mudstone. They have medium-high TOC content and variable sedimentary textures. The reservoir porosity varies between 2% and 10%, with a mean of 5.3%, and the permeability is less than 0.1mD (Li et al., 2020).
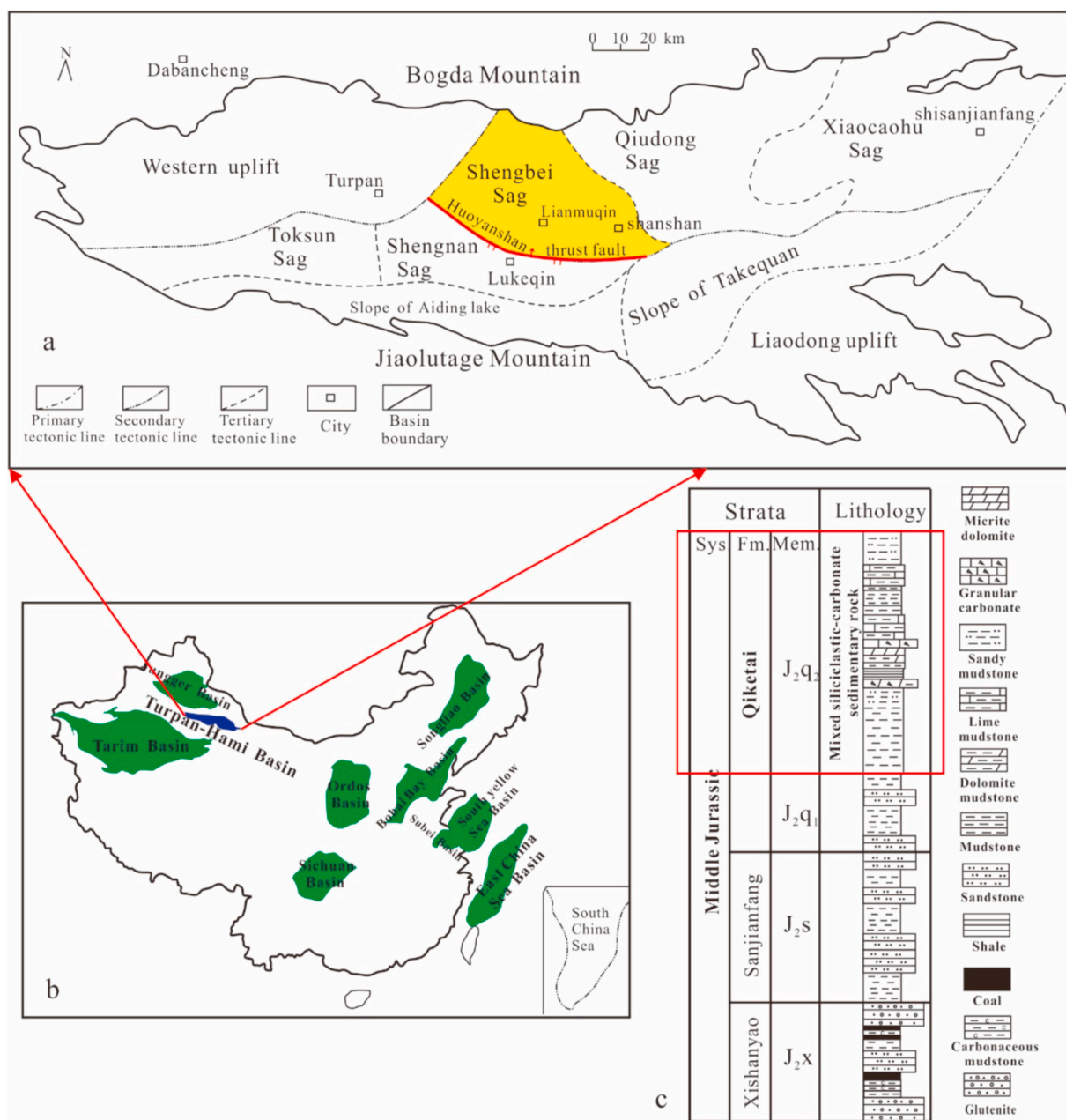
Fig. 1. (a) Geographic location of the Shengbei sag. (b) Geographic location of the Turpan-Hami Basin in China. (c) Simplified stratigraphic units of the Middle Jurassic in the Shengbei Sag.

3. Samples and experimental methods

A total of 14 lacustrine organic-rich tight rock samples were obtained from the J_2q_2 Member in the Shengbei Sag. X-ray diffraction (XRD) analysis, thin sections observation, FE–SEM imaging, Rock-Eval Pyrolysis, and low-temperature N_2 absorption were all conducted on all samples. Eight samples were selected for NMR core analysis with high-speed centrifuge.

3.1. Experimental methods

The experimental analysis of TOC and Rock-Eval Pyrolysis were conducted in the petroleum geology laboratory, China University of Petroleum (Beijing). Powdered samples are treated with 5% of HCl to remove inorganic carbon, then rinsed with deionized water several times, and the samples were dried at 80 °C for 12 h, then 0.1 g of dried

powder is measured by LECO CS230 carbon/sulfur analyzer. The T_{max} (the temperature at which the maximum amount of S_2 hydrocarbons are generated; Peters, 1986) were obtained by Rock-Eval Pyrolysis. The experiment was performed by Rock-Eval OGE-II instrument following the Chinese National Standard GB/T 18,602–2012.

The mineralogical composition was determined using X-ray diffraction (XRD) analysis. The samples were crushed into powder (200 mesh), and then they were analyzed on Bruker D2 PHASER X-ray diffractometer with Cu-Kα radiation. The pattern was recorded over a 2θ interval of 4.5°–50°, with a step size of 2°. The test method was in accordance with the Chinese Oil and Gas Industry Standard SY/T 5163–2010. Subsequently, the quantitative mineralogy of samples was obtained by analyzing the spectra with relative intensity ratio (RIR) method based on the principles from Chung (1974a, b).

Leica DM4500P fluorescence microscope was used to observe and characterize the lithology and sedimentary texture of the samples. FEI

Quanta 200 scanning electron microscope (SEM) with an energy dispersive X-ray spectrometer (EDS) was used to observe the pore morphology. These samples were cut into the size of 1 cm × 1 cm × 5 mm, and polished using broad argon-ion beam (BIB). The operating conditions are as follow: resolution <1.2 nm, beam voltage 200 V- 30 kV, high vacuum scanning mode.

Low-temperature N_2 adsorption was measured at −196 °C (77.3 K). The crushed samples (60–80 mesh) were de-watered in a dry oven at 80 °C for 4 h, and then desorbed gases and volatiles under vacuum at 150 °C for 12 h, before the N_2 adsorption was performed with a Micromeritics ASAP 2460 Surface Area and Porosity Analyzer. The adsorption-desorption isothermal curve is obtained from the relative pressure P/P_0 as the horizontal axis and the absorptive capacity per unit mass as the ordinate. Then, according to the hysteresis loop formed by the adsorption-desorption isothermal curve, the pore morphology was determined. Meanwhile, the specific surface area (SSA) was following the Brunauer-Emmett-Teller (BET), the pore volume was calculated following the Barrett-Joyner-Halenda (BJH) model. Further, the pore size distribution was calculated by the technique of BJH (Brunauer et al., 1938; Barrett et al., 1951).

The experiments of water-saturated and centrifugal nuclear magnetic resonance (NMR) were carried out by the Mesomr23-060-h-i NMR instrument. Testing conditions are as follows: 21 MHz resonance frequency, probe coil with diameter of 25 mm, sampling sequence of T_2 value is CPMG, the minimum echo time spacing of TE = 0.1 ms. All samples were cut into 2.5 cm × 3 cm plugs, after drying for 48 h at 60 °C, then putting into water-saturated device, vacuum-pumping for 2 h, saturated water for 12 h under 15Mpa, and then NMR T_2 spectra were measured by NMR analyzer. The samples are centrifuged for 12 h at 500 psi until no movable fluid remained. Finally, T_2 spectra were obtained after centrifugation.

3.2. Fractal theory

Fractal dimensions have been considered as a reliable and useful parameter to characterize pore structure and its irregular surface quantitatively (Liu and Ostadhassan, 2017; Pour and Li, 2016; Huang et al., 2017). Generally, fractal dimension (D) is between 2 and 3, which is mainly influenced by complexity and irregularity of pore surface. The value of 2 is regarded as an extremely smooth surface and the value of 3 refers to a rough surface with irregular topography and space filling surface (Jaroniec et al., 1995; Yang et al., 2016). The methods for calculating the fractal dimensions mainly include high-pressure mercury injection, N_2 adsorption, FE-SEM imaging and nuclear magnetic resonance (Wang et al., 2015; Sun et al., 2016).

3.2.1. Fractal dimensions based on N_2 adsorption isotherms

The low-temperature N_2 adsorption is an important analysis method to quantitatively describe the irregularity and heterogeneity of pore structure in unconventional reservoir (Pfeifer and Ismail, 1994; Shao et al., 2017). Based on N_2 adsorption isotherms, most scholars usually use Frenkel-Halsey-Hill (FHH) fractal model to calculate the fractal dimension for fine-grained sedimentary rocks and characterize the heterogeneity of pore structure (Avnir and Jaroniec, 1989; Huang et al., 2017). The calculation formula of FHH model is as follows:

$$\ln V \Big/ V_0 = f(D)\ln\ln\frac{P_0}{P} + C \tag{1}$$

where V is the adsorbed volume under equilibrium pressure P, cm^3/g; V_0 is the monolayer coverage volume; P_0 is the saturation pressure; f(D) is the expression of the fractal dimension;

When the adsorbed force is van der Waals force mainly, the relationship between f(D) and fractal dimension is:

$$f(D) = \frac{D-3}{D} \tag{2}$$

When the adsorbed force is surface tension mainly, the correlations between f(D) and fractal dimension is as follow:

$$f(D) = D - 3 \tag{3}$$

f (D) is the slope of Equation (1).

3.2.2. Fractal dimensions from NMR

Pore structure and its fractal dimension obtained from NMR analysis have been widely used in shale and tight reservoirs, and achieved considerable achievements (Pfeifer and Ismail, 1994; Shao et al., 2017). The fractal model based on NMR can be described as:

$$\lg V = (3 - D)\lg T_2 + (D - 3)\lg T_{2max} \tag{4}$$

where T_{2max} is the maximum T_2 relaxation time, ms; V is the accumulative pore volume fraction (%) ($T_2 < T_{2max}$); D is the fractal dimension. In the plot of $\lg V$ versus $\lg T_2$ based on NMR data, the curve has two different linear phases in the whole T_2 relaxation time range, and have a good linear correlation. Fractal dimensions D be calculated by the slope of equation (4).

4. Results

4.1. Mineralogical components, TOC content, sedimentary structure, and rock types

The lacustrine organic-rich fine-grained mixed siliciclastic-carbonate sediments of J_2q_2 are characterized by complex mineralogical compositions and sedimentary structures. Three rock types with different sedimentary textures and mineralogical compositions were identified using thin sections (Fig. 2). The first rock type is a silt-bearing argillaceous micritic dolomite with no obvious sedimentary textures (Fig. 2a and b), which was defined as Type RI. There was some dispersed organic matter throughout the matrix (Fig. 2b). The SEM analysis revealed the presence of intercrystalline pores among the dolomite rhombs, and some of the pores are filled by clay and silicate minerals (quartz and feldspar) (Fig. 2c). According to the thin section observations, samples Th7, Th8 and Th12 are silt-bearing calcitic dolomite with a large amount of intraclasts, which was defined as Type RII. The intraclasts mainly exhibit spot -line grain contacts, their size reaches the sand-gravel level, and the pores between the intraclasts are filled with sparry calcite cement (Fig. 2d and e). The intraclasts are composed of micritic dolomite and ankerite. Based on the observation of SEM, deformed OM and clay minerals fill the dolomite intercrystalline pores (Fig. 2f). Samples Th3, Th4, Th11, and Th 13 are silt-bearing argillaceous micritic limestone with an obvious laminated texture (Fig. 2g and i), which was defined as Type RIII. The micritic carbonate is interbedded with dark organic-rich argillaceous siltstone. Micritic calcite or dolomite are dominant in the lighter laminae, and the boundary of the laminas are slightly fuzzy and fluctuant (Fig. 2h). In addition, some organic matters fill the interparticle pores, which can be observed under the field emission scanning electron microscopy (FE-SEM) of argon-milled thin sections (Fig. 2i).

The X-ray diffraction (XRD) data are shown in Table 1 and Table 2. The major minerals include quartz, feldspar, and carbonate minerals, followed by clay minerals. The types of clay minerals include kaolinite, chlorite, illite and illite/smectite mixed layer. The identified rock types exhibit different mineralogical compositions and different types of clay minerals (Peters et al., 2005; Burton et al., 2019). The silt-bearing argillaceous micritic dolomite (Type RI) has moderate contents of quartz, feldspar and carbonate minerals, the silicate minerals (quartz and feldspar) content ranges from 23 to 57 wt% with an average of 39 wt%; the carbonate content is 37–56 wt%, with an average of 43 wt%; and the dolomite content (average of 26 wt%) is slightly higher than calcite content (average of 17 wt%). In addition, the clay mineral content is between 5 wt% and 30 wt% with a mean value of 15 wt%, the main types of clay include chlorite and illite/smectite mixed layer. The
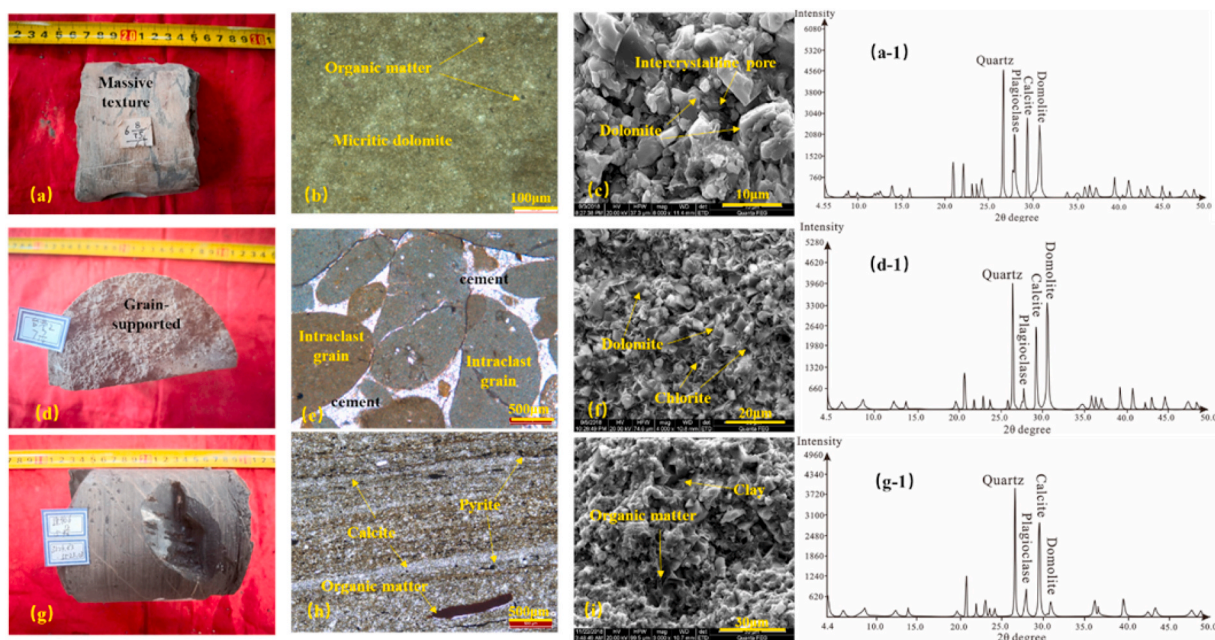
Fig. 2. (a) Type RI, the core image of sample Th5, silt-bearing argillaceous micritic dolomite, grayish brown, massive texture; (b) The microscopic image of sample Th5, micritic dolomite with no obvious sedimentary texture, organic matter is dispersed in the matrix; (c) The SEM image of sample Th5, dolomite rhombs with 5–10 μm crystal size and intercrystalline pore. (a-1) the XRD peak data of sample Th5; (d) Type RII, the core image of sample Th7; (e) The microscopic image of sample Th7, well-sorted intraclasts with spot - line grain contact, intergranular sparry calcite cement; (f) The SEM image of sample Th7, a large number of rhombic dolomites were observed, intercrystalline chlorite; (d-1) The XRD spectrogram of sample Th7; (g) Type RIII, the core image of sample Th4, laminated silt-bearing argillaceous micritic limestone, dark grey; (h) The microscopic image of sample Th4, the light lamina is composed of micritic calcite, the dark lamina is composed of organic-rich argillaceous siltstone and clay, pyrites are distributed along the lamina; (i) The SEM image of sample Th4, organic matter and clay fill in interparticle pores; (g-1) The XRD spectrogram of sample Th5. (For interpretation of the references to colour in this figure legend, the reader is referred to the Web version of this article.)

Table 1
Mineralogical compositions, TOC contents and the maturity (Tmax and Vitrinite reflectance Ro) values of the tight reservoir samples.

Sample ID	Rock types	Depth/ m	Clay (%)	Quartz (%)	Feldspar (%)	Calcite (%)	Dolomite (%)	Ankerite (%)	Analcite (%)	Pyrite (%)	Hematite (%)	TOC (%)	Tmax (°C)	Ro (%)
Th1	Type RI	3646.5	20	12	19	14		23	13			0.12	436	0.66
Th2	Type RI	3486.2	30	18	5	10	30		8			0.37	439	0.72
Th3	Type RIII	3521.9	12	23	11	45	6			3		8.00	437	0.68
Th4	Type RIII	3524.3	22	20	5	35		17		1		2.68	439	0.72
Th5	Type RI	3852.0	5	22	29	21	23					4.38	441	0.75
Th6	Type RI	3863.9	5	25	32	16	23					7.56	441	0.75
Th7	Type RII	3889.8	10	31	6	23	30					0.55	440	0.73
Th8	Type RII	3489.6	8	22	10	45		15				2.80	440	0.73
Th9	Type RI	3825.2	11	38	8	21	22					0.14	440	0.73
Th10	Type RI	3887.9	16	20	6	20		36			2	0.80	444	0.81
Th11	Type RIII	3526.8	22	20	6	51		1				3.50	441	0.75
Th12	Type RII	3489.4	22	17	5	27	26			2		2.49	440	0.73
Th13	Type RIII	3504.4	18	33	21	10			17		1	0.26	435	0.64
Th14	Type RI	3510.7	12	32	13	32	8		3			5.30	436	0.66

Type RI: Silt-bearing argillaceous micritic dolomite; Type RII: silt-bearing calcitic dolomite with a large amount of intraclasts; Type RIII: silt-bearing argillaceous micritic limestone.

Table 2
The main types of clay mineral in the tight reservoir samples.

Sample ID	Rock Type	Depth/m	Clay (%)	Kaolinite (%)	Chlorite (%)	illite (%)	Illite/smectite mixed layer (%)
Th2	Type RI	3486.2	30	3	3	15	79
Th4	Type RIII	3524.3	22	26	21	18	35
Th9	Type RI	3825.2	11	10	24	21	45
Th11	Type RIII	3526.8	22	20	19	37	24
Th12	Type RII	3489.4	22	6	20	21	53

silt-bearing calcitic dolomite with a large amount of intraclasts (Type RII) has low clay content, the carbonate content is between 53 wt% and 60 wt% with a mean value of 55 wt%; the dolomite content is similar to the calcite content; and the average content of the silicate minerals and clay minerals are 30 wt% and 13 wt%, respectively. The clay minerals are mainly composed of illite and illite/smectite mixed layer. For the silt-bearing argillaceous micritic limestone (Type RIII), the silicate minerals content ranges from 25 wt% to 54 wt% with an average of 37 wt%; the carbonate content is between 10 wt% and 52 wt%, with a mean value of 41 wt%; and the calcite content is significantly higher than the dolomite content. Moreover, the average contents of the clay minerals and pyrite are 17 wt% and 2 wt%, respectively, which are slightly higher than those of the other rock types. In addition, the kaolinite content of Type RIII is obviously higher than that of other rock types.

The TOC of the studied samples range from 0.12% to 8.0%, with a mean value of 2.78% (Table 1). Type RI, which includes six samples (Th1, Th2, Th5, Th6, Th9, and Th10), has a moderate TOC content, with an average value of 2.22 wt%. Type RII, which included three samples (Th7, Th8 and Th12), has a low-moderate TOC content (<2.0 wt%). The TOC contents of Type RIII are significantly higher than other rock types. The T_{max} values are between 435 °C and 444 °C, with an average of 439 °C, suggesting organic-rich mixed siliciclastic-carbonate rocks are in the stage of low maturity (Feng et al., 2019). Using the relationship between T_{max} and Ro reported by Jarvie et al. (2007), the Ro values calculated from the T_{max} values are 0.64–0.81%, with an average value of 0.72% showing that most of the samples are in low maturity stage. However, it should be noted that such T_{max}-based estimates would benefit from additional methods of investigation, such as maturity estimates based on biomarker and diamondoid analysis (e.g., Dahl et al., 1999; Peters et al., 2005; Burton et al., 2018) as well as estimates derived from basin modeling approaches (e.g., Waples et al., 1992; Hantschel and Kaueauf, 2009; Opera et al., 2013).

4.2. Pore morphology characteristics

The pore morphology of the tight reservoir, including the size, shape, and connectivity of the pores, was determined based on SEM observations of argon-milled thin sections. Based on the classification scheme of pore types proposed by Loucks et al. (2012), the pores in the fine-grained mixed siliciclastic-carbonate rocks were divided into intraparticle, interparticle, and OM. The interparticle pores were commonly observed among the rigid particles or crystals, which tend to form effective pore networks due to their good connectivity. The intraparticle pores were generally observed within the particles or crystals, and their connectivity is generally poor. The OM pores were commonly observed within the interior or at the edges of the organic matter, their development may be related to the maturity of organic matter (Li et al., 2019b). As is shown in Fig. 3a–h, a large number of nanoscale interparticle pores were observed in the samples, including the interparticle pores between carbonate minerals. Among them, the dolomite intercrystalline pores are the most developed and the dolomites have a weak dissolution. The pore sizes are generally less than 200 nm, with morphologies including isolated plate-shaped, irregular circles or ellipsoids (Fig. 3a, c, d, e). In addition, some of the interparticle pores are filled with ductile OM and clay minerals (Fig. 3c, e), and narrow grain-rim interparticle pores were observed between the ductile organic matter and the rigid particles.

These pores are commonly elongated and regular (Fig. 3b, g). A small number of intraparticle pores were observed in the samples, including pores within the calcite, dolomite, and clay minerals (Fig. 3f, h). These pores generally exhibit ink-bottle shapes or irregular ellipsoid shapes, with small pore sizes and poor connectivity. Moreover, nanometer scale micro-fractures were also observed in the samples, mainly including shrinkage fractures in clay rock matrix (Fig. 3g). Based on the statistics of 50 FE-SEM images of 14 samples (Fig. 3i), the main pore types were inorganic mineral interparticle pores (dolomite and calcite intercrystalline pores) and the organic matter pores were very poorly developed.

Most of the samples from the study area are in the low-maturity stage. In general, in the early stage of the oil generation window, organic matter has a low capacity for hydrocarbon generation (Curtis et al., 2012). Therefore, the OM pores are poorly developed in the studied tight reservoir samples. This is different from the Longmaxi marine shales, which contain a large number of OM pores if the Longmaxi marine shales have higher maturity (Liang et al., 2019). According to investigations of the marine shales in North America, it is believed that the development degree of the OM pores in shales is mainly influenced by the OM abundance and maturity (Wang et al., 2018). However, large numbers of OM related pores are only observed when the organic matter maturity is high with a Ro value greater than 1.1%. After which, as the total organic carbon content increases, the organic matter maturity increases, and the volume and internal specific surface area of the organic matter pores grow. Therefore, in organic-rich rocks with a low maturity, most of pores are interparticle and occur between the carbonate or silicate crystals or debris.

4.3. Quantitative analysis of the pore structure

4.3.1. Low-temperature N_2 adsorption isotherms (LTNA)

In order to the comprehensive characterization of the pore structure, low-temperature N_2 adsorption was employed for all studied samples. The obtained results can reveal the pore ranges of 2–100 nm, the shape of the hysteresis loop and the contributions of different scales to TPV and SSA (Yang et al., 2014; Yang et al., 2016; Li et al., 2019b). The adsorption isotherm is a function of the adsorption volume under the pressure at a certain temperature (Yang et al., 2016). As shown in Fig. 4 (samples Th1–14), the N_2 adsorption isotherms of all of the samples have a reversed S-shape, which belong to type IV based on the International Union of Pure and Applied Chemistry (IUPAC) classification (Sing, 1985). The N_2 adsorption isotherms of All the studied samples exhibit obvious hysteresis loops. The possible reason for the hysteresis loop was that capillary condensation occurred in the mesopores, indicating that the tight reservoir samples have abundant mesopores (2–50 nm; Sing, 1985). For the adsorption branch of the organic-rich fine-grained mixed siliciclastic-carbonate rocks with low maturity, when the relative pressure (P/P$_0$) is less than 0.95, the curve increases slowly with increasing P/P$_0$, suggesting that the adsorption mainly occurred in the micropores-mesopores (2–50 nm). When P/P$_0$ approaches 1.0, the curve rises rapidly, but saturation does not occur, indicating that the sample may contain a small number of macropores (Gregg and Sing, 1982). For the desorption branch, when P/P$_0$ > 0.45, the adsorption and desorption isotherms do not completely overlap, and the desorption branch is above the adsorption curve. When P/P$_0$ approaches 0.45, the curve drops rapidly, and then it overlaps with the adsorption curve.
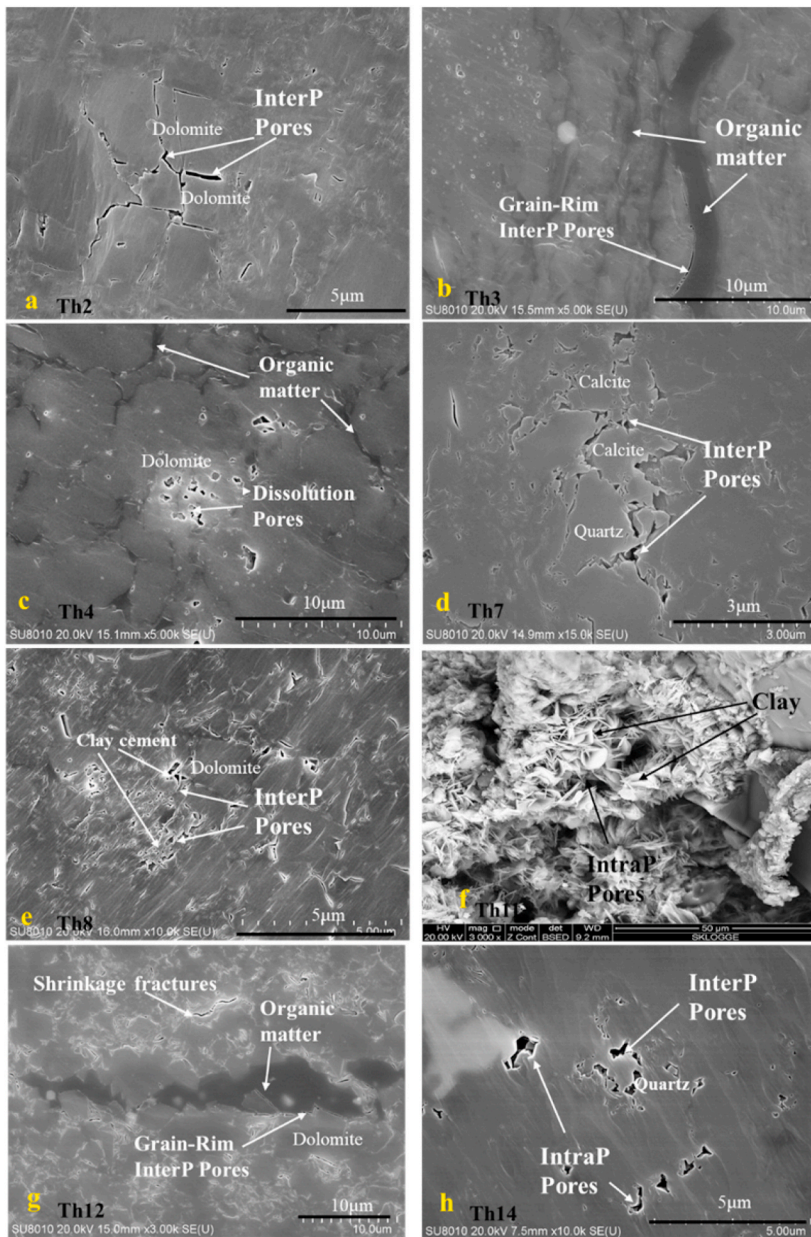
Fig. 3. Examples of interparticle and intraparticle pores within the mixed siliciclastic-carbonate rocks. (a) The SEM image of sample Th2, the interparticle pores among the dolomite rhombs, are plate-like or slit-shaped; (b) The SEM image of sample Th3, dark band of organic matter, and narrow grain-edge OM pores located between the ductile organic matter and rigid particles; (c) The SEM image of sample Th4, intraparticle dissolution pores within dolomite, the interparticle pores are filled with organic matter; (d) The SEM image of sample Th7, interparticle pores between calcite and quartz; (e) The SEM image of sample Th8, dolomite interparticle pores with poor connectivity, and complexity and irregularity. Clay minerals filled interparticle pores; (f) The SEM image of sample Th11, illite/smectite mixed layer, and interparticle pores between clay crystals; (g) The SEM image of sample Th12, and some shrinkage fractures; (h) The SEM image of sample Th14, the ink-bottle-shaped intragranular pores. (i) The statistical results of pore types from SEM images of the studied samples.
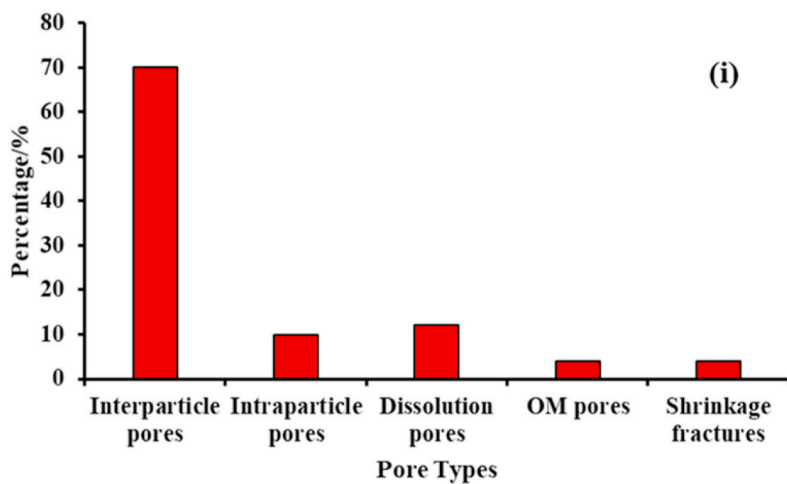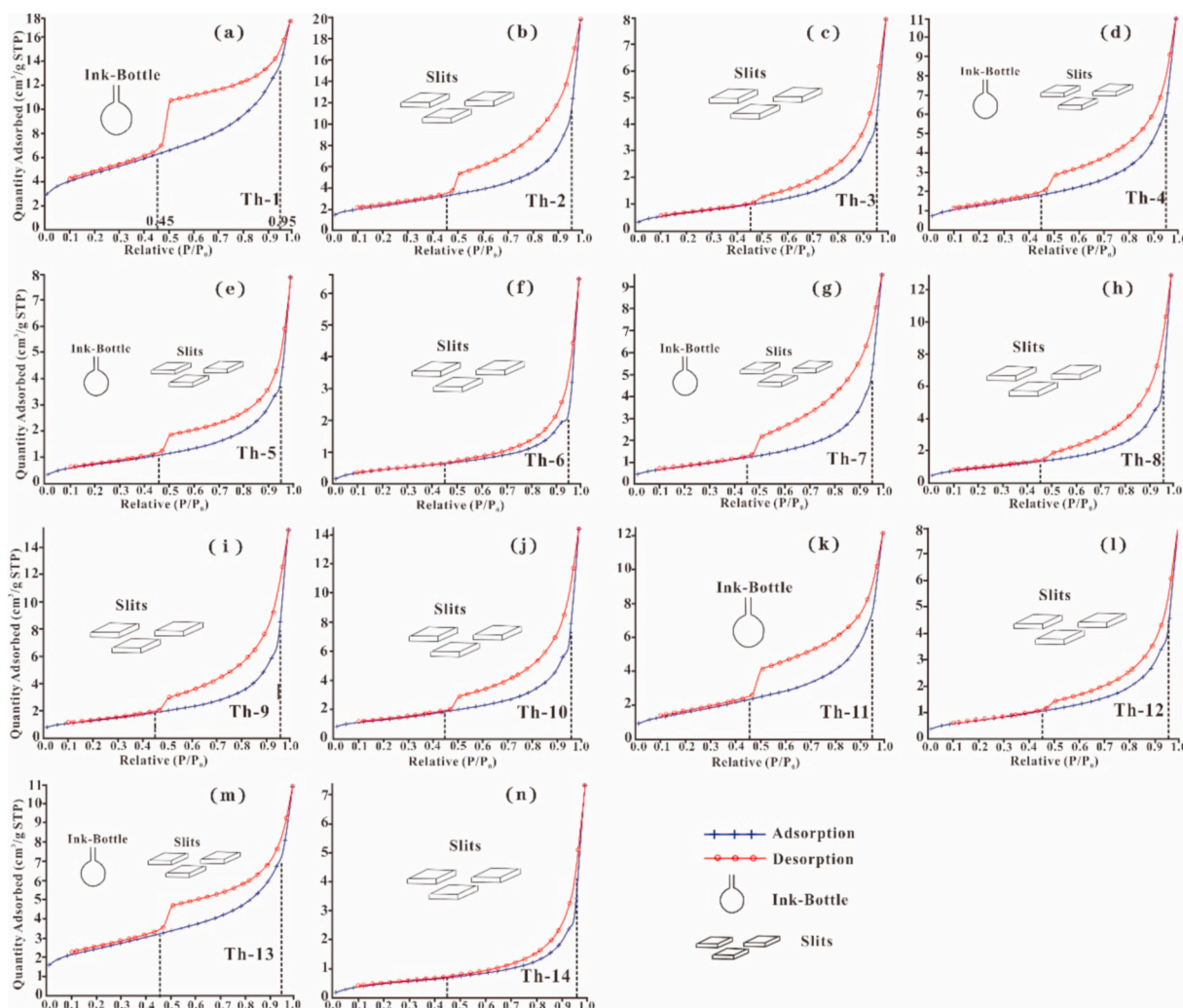
Fig. 4. N₂ adsorption and desorption isotherms of mixed siliceous-carbonate sedimentary rock samples. (a) Sample Th-1, type H2, ink-bottle-shaped pores; (b) Sample Th-2, type H3, slit-shaped pores; (c) Sample Th-3, type H3, slit-shaped pores; (d) Samples Th-4, mixed type, a mixture of slit-shaped and the ink-bottle-shaped; (e) Sample Th-5, mixed type, a mixture of slit-shaped and the ink-bottle-shaped; (f) Sample Th-6, type H3, slit-shaped pores; (g) Sample Th-7, mixed type, a mixture of slit-shaped and the ink-bottle-shaped; (h) Sample Th-8, type H3, slit-shaped pores; (i) Sample Th-9, type H3, slit-shaped pores; (j) Sample Th-10, type H3, slit-shaped pores; (k) Sample Th-11, type H2, ink-bottle-shaped pores; (l) Sample Th-12, type H3, slit-shaped pores; (m) Sample Th-13, mixed type, a mixture of slit-shaped and the ink-bottle-shaped; (n) Sample Th-14, type H3, slit-shaped pores. The IUPAC classification of the hysteresis loop are from Sing (1985)..

Following the IUPAC classification of the hysteresis loop (Sing, 1985), the hysteresis loops of 14 tight reservoir samples are mainly classified into three types: type H2, type H3, and a mix of types H2 and H3 (Fig. 4). The type H2 loop corresponds to pores with narrow necks and wide bodies (ink-bottle-shaped pores), whereas type H3 is associated with aggregates of plate-like particles giving rise to slit-shaped pores. In addition, the hysteresis loops of some of the samples are not typical type H2 or type H3, because their shapes are between types H2 and H3. The possible reason for this is that the mixed siliciclastic-carbonate rocks in the study area have a complex mineralogical composition and pore structure, so they may be a comprehensive reflection of several pore structure types. As is shown in Fig. 4, the hysteresis loops of samples Th1 and Th11 are type H2 (Fig. 4a and k), indicating that ink-bottle-shaped pores prevail in these samples. The hysteresis loops of samples Th2, Th3, Th6, Th8, Th9, Th10, Th12, and Th14 are similar to type H3 loops, suggesting that slit-shaped pores are dominant in these samples (Fig. 4b, c, f, h, i, j, l, n). Nevertheless, the hysteresis loops of the other samples (Th4, Th5, Th7 and Th13) mainly exhibit type H3 loops with some features of type H2 loops, suggesting that the pore shapes in these sample are a mixture of slit-shaped and ink-bottle-shaped (Fig. 4d, e, g, m). The above analysis results show that

Table 3
The analysis results of low-temperature N₂ isothermal adsorption of all samples.

Sample ID	Rock types	Depth (m)	BET SSA/ m²/g	BJH TPV/cm³/ 100 g	APD/ nm
Th1	Type RI	3646.5	8.556	2.380	7.63
Th2	Type RI	3486.2	8.158	3.000	16.19
Th3	Type RIII	3521.9	2.473	1.233	18.37
Th4	Type RIII	3524.3	4.575	1.690	14.38
Th5	Type RI	3852.0	2.659	1.520	16.86
Th6	Type RI	3863.9	1.707	1.203	21.85
Th7	Type RII	3889.8	3.024	2.480	17.57
Th8	Type RII	3489.6	3.332	1.990	21.81
Th9	Type RI	3825.2	4.522	2.220	19.56
Th10	Type RI	3887.9	5.839	1.860	12.76
Th11	Type RIII	3526.8	2.637	1.230	17.09
Th12	Type RII	3489.4	4.602	2.370	19.39
Th13	Type RIII	3504.4	6.397	1.570	7.99
Th14	Type RI	3510.7	1.833	1.130	23.95

slit-shaped pores and mixed-type pores prevail in the studied samples.

As is shown in Table 3, the BET SSA, the BJH TPV and APD were obtained from LNTA analysis. For Type RI, the BET SSA ranges from

1.707 m²/g to 8.556 m²/g with an average value of 4.753 m²/g; the BJH TPV is between 1.203 cm³/100 g and 3.000 cm³/100 g, with an average value of 1.902 cm³/100 g; and the average pore diameter (APD) ranges from 7.63 nm to 23.95 nm with an average value of 16.97 nm. Type RII has high TPV and APD values; the BET SSA values range from 3.024 m²/g to 4.602 m²/g, with a mean of 3.653 m²/g; the BJH TPV values range from 1.99 cm³/100 g to 2.48 cm³/100 g, with an average value of 2.28 cm³/100 g; and the APD values range from 17.57 nm to 21.81 nm, with an average value of 19.59 nm. For Type RIII, the BET SSA ranges from 2.473 m²/g to 6.396 m²/g, with a mean of 4.020 m²/g, the BJH TPV ranges from 1.230 cm³/100 g to 1.690 cm³/100 g, with an average value of 1.431 cm³/100 g; and the APD ranges from 7.99 nm to 18.37 nm, with an average value of 14.46 nm. The pore size distribution curves for all 14 tight reservoir samples shown in Fig. 5. These curves were constructed using the BJH model. Most of the samples have similar pore size distribution characteristics, and their pore sizes have a wide range of 2

nm–100 nm. The pore size distribution curves of the samples Th3, Th7, Th8, Th9, Th12, and Th14 are bimodal, with a major peak occurring at around 2–4 nm and another peak at around 6–35 nm (Fig. 5c, g, h, i, l, n). The pore size distribution curves of the other samples exhibit unimodal pattern, with a main peak at around 2–4 nm (Fig. 5a, b, d, e, f, j, k, m).

As is shown in Table 4, compared with marine shales, the hysteresis loop types of the adsorption-desorption curves of marine-continental transitional shales, mature lacustrine shales, and lacustrine tight carbonate rocks are similar (types H2 and H3), whereas their pore size distributions are slightly different. The BJH TPV and APD values of low-maturity organic-rich tight reservoirs are significantly larger than those of transitional shales (Li et al., 2019b); however, they are significantly lower than those of the Niutitang marine shale in the Sichuan Basin and the Mississippi Barnett shale (Yang et al., 2016; Clarkson et al., 2013). Additionally, their BET SSA values are also lower than those of marine
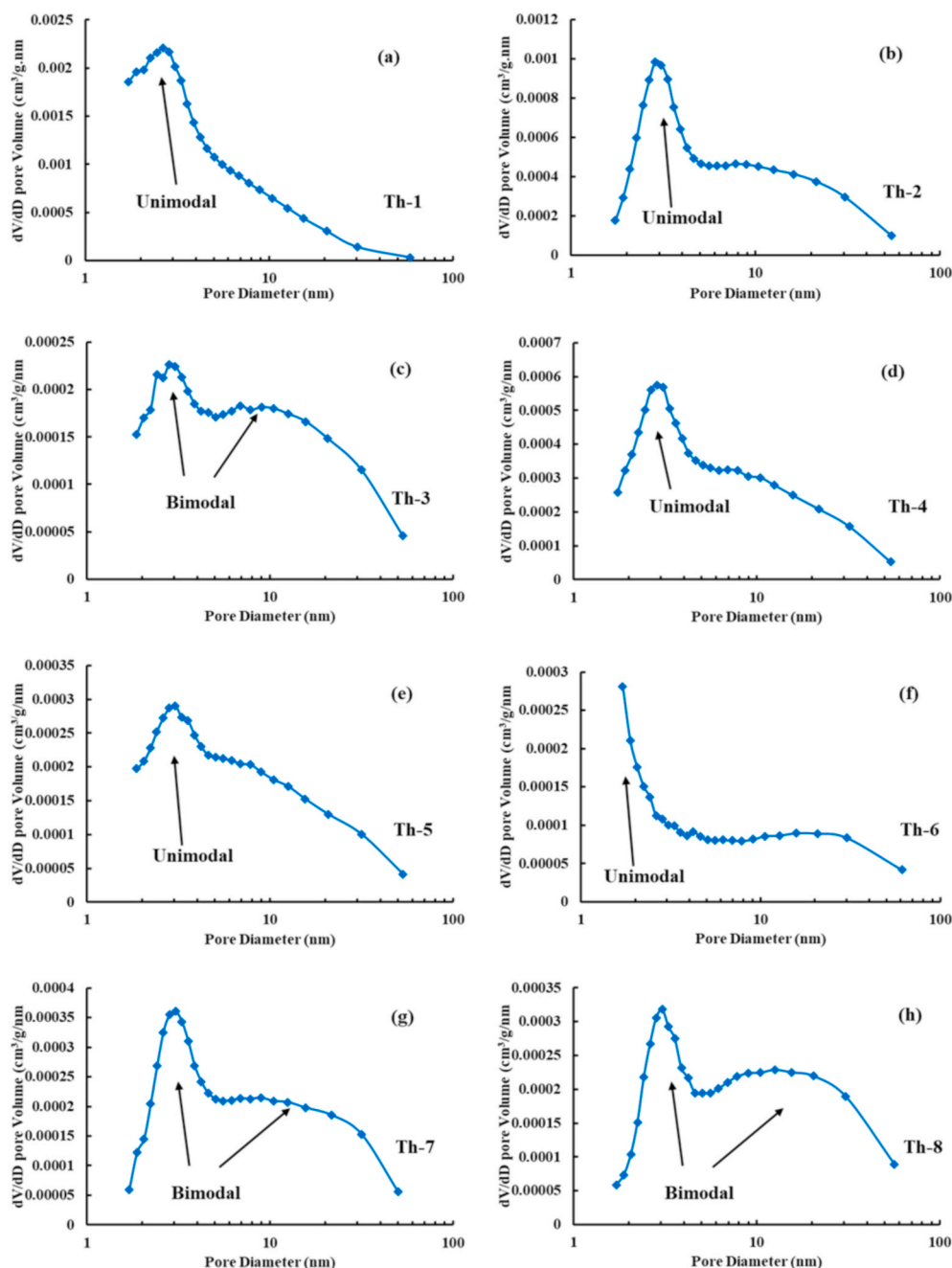

Fig. 5. Pore size and distributions obtained from low-temperature N₂ adsorption isotherms. (a) Sample Th1, Type RI, unimodal distribution; (b) Sample Th2, Type RI, unimodal distribution; (c) Sample Th3, Type RIII, bimodal distribution; (d) Sample Th4, Type RIII, unimodal distribution; (e) Sample Th5, Type RI, unimodal distribution; (f) Sample Th6, Type RI, unimodal distribution; (g) Sample Th7, Type RII, bimodal distribution; (h) Sample Th8, Type RII, bimodal distribution; (i) Sample Th9, Type RI, bimodal distribution; (j) Sample Th10, Type RI, unimodal distribution; (k) Sample Th11, Type RIII, unimodal distribution; (l) Sample Th12, Type RII, bimodal distribution; (m) Sample Th13, Type RIII, unimodal distribution; (n) Sample Th14, Type RI, bimodal distribution.
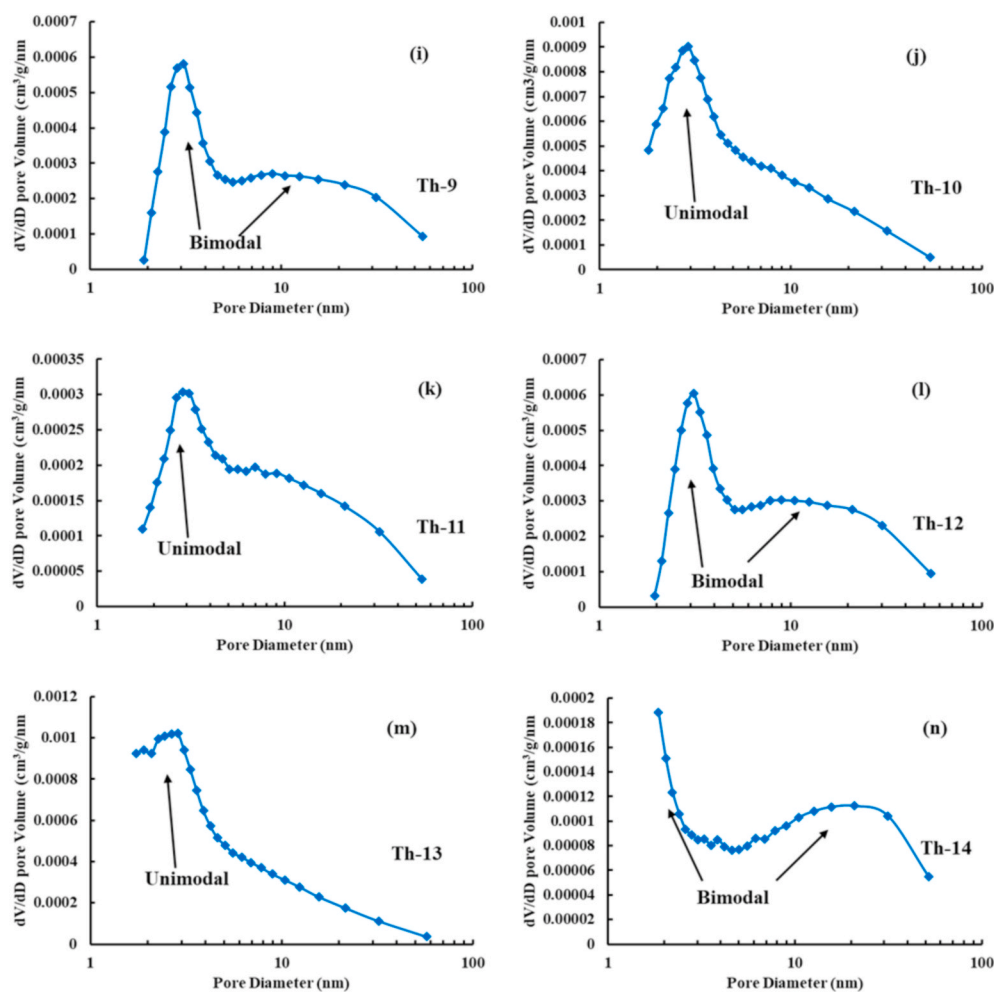
Fig. 5. (*continued*).

Table 4
Comparisons of pore structure parameters obtained from LTNA between mixed siliciclastic-carbonate sedimentary rock and other fine-grained rocks.

No.	Lithology	Location	Strata	BET SSA(m²/g)	BJH TPV (cm²/100 g)	APD (nm)	Hysteresis loops types	References
1	Fine-grained mixed siliciclastic-carbonate sedimentary rocks	Turpan-Hami Basin	Middle Jurassic Qiketai Formation	1.707–8.556 (4.31)	1.13–3.0 (1.848)	7.63–23.95 (16.82)	H2,H3	This paper
2	Lacustrine carbonate	Sichuan Basin	Jurassic Da'anzhai member	4.32–9.25 (6.02)	1.79–3.89 (2.50)	15.25–19.81 (17.56)	H3	Xu et al. (2019)
3	Lacustrine shale	Songliao Basin	Upper Cretaceous Qingshankou Formation	0.39–34.06 (10.92)	0.13–4.18 (1.59)	3.16–16.48 (9.56)	H2,H3	Wang et al. (2015)
4	Lacustrine shale	Ordos Basin	Upper Triassic Chang 7 member	0.25–4.39 (2.62)	0.02–0.90 (0.49)	6.67–18.40 (11.23)	H3	Jiang et al. (2016)
5	Low mature lacustrine shale	Bohai Bay Basin	Paleogene Kongdian Formation	0.228–9.126 (2.22)	0.154–2.485 (0.778)	10.15–26.24 (17.98)	H2,H3	Chen et al. (2019)
6	Marine Shale	The Southern Sichuan Basin	Lower Cambrian Niutitang Formation	9.4–33.9 (20.68)	1.54–5.11 (3.25)	3.8–10.03 (8.06)	H2,H3	Yang et al. (2014)
7	Maine-continental shale	East margin of Ordos Basin	Upper Paleozoic	1.071–10.082 (8.6)	0.05–1.56 (0.91)	4.33–11.89 (7.08)	H2,H3	Li et al. (2019b)

shale and transitional shale. Compared with the Kongdian lacustrine low-maturity shale in the Cangdong Sag (Chen et al., 2019), the tight reservoirs in J_2q_2 have high BJH TPV and BET SSA values and similar average pore diameters (APD). Moreover, the pore structure parameters of the mixed siliciclastic-carbonate reservoirs are also slightly lower than those of the tight lacustrine carbonate rocks of the Jurassic Da'anzhai Formation in the Sichuan Basin (Xu et al., 2019). However, compared with the mature lacustrine shale with high TOC contents

(Wang et al., 2015; Jiang et al., 2016), the mixed siliciclastic-carbonate reservoirs have higher BJH TPV and APD values and lower BET SSA values. These results suggest that the rock type, mineralogical composition, and organic matter content have important effects on pore structure.

4.3.2. NMR T_2 spectrum distributions
Generally, NMR is suitable for characterizing the pore structures

ranging in size of 2 nm–10 μm (Huang et al., 2017; Xu et al., 2019). The characteristics of pores or fractures can be evaluated by the characteristics of the transverse relaxation time T_2 peaks. Peaks (left peak) with low T_2 values reflect small pores, peaks (right peak) with high T_2 values reflect large pores or fracture (Fig. 6a). The area of the peak reflects the number of pores or fractures, the zone between the right peak and left peak reflects the pores connectivity (Testamanti and Rezaee, 2017; Xu et al., 2019).

The NMR T_2 spectra for eight samples are illustrated in Fig. 6. The distributions of the NMR T_2 spectra of most of the samples are similar. According to the distribution characteristics of the NMR T_2 spectra under water-saturated conditions, the pore size distribution patterns of all eight samples can be divided into two models. The first model (samples Th1, Th4, Th9, Th12, and Th13) is bimodal with a major peak (P1) around 0.03–1 ms and another peak (P_2) around 10–100 ms (Fig. 6a, c, e, f, h). However, the amplitude of the zone between peaks P_1 and P_2 is quite low, which is close to 0. In addition, the peak P_2 of sample Th13 is wider and larger than that of the other samples, which is likely because this sample contains micro-cracks (Fig. 6h). The second model (samples Th3, Th8, and Th11) show obvious left unimodal characteristics, and the area of the right peak (P_2) is close to 0 (Fig. 6b, d, f). Therefore, the distribution characteristics of the NMR T_2 spectra of the samples indicate that the mixed siliciclastic-carbonate sedimentary rock reservoirs are mainly dominated by relatively small pores (nanoscale

absorbed pores), and only some of the samples have a small number of larger pores. In addition, the connectivity between the pores represented by peaks P_1 and P_2 is very poor. The percentages of the mobile fluid (Sm) were quantitatively obtained through centrifugal NMR analysis. All of the samples exhibited left unimodal pattern at centrifugal forces of greater than 500psi, and the amplitude was significantly lower than water-saturated conditions (Fig. 6a-m). These results indicate that there are also some movable fluids in the small pores, but the bound fluids are still dominant. As is shown in Fig. 6 and Table 5, the boundary value between the moveable and bound fluids is 0.5 ms (T_2 cutoff), which approximately corresponds to the pore-throat threshold of 0.025 μm (Li et al., 2020). According to this threshold value, the bound fluid saturation is high and ranges from 54.7% to 93% with a mean of 76.9%, and the mobile fluid saturation is generally low (<35%). This indicates that the pore connectivity of the mixed siliciclastic-carbonate sedimentary rock reservoirs is poor. However, the mobile fluid saturation of sample Th13 is greater than 45%, which is significantly higher than tight sandstone (Shao et al., 2017). This is likely due to the presence of micro-fractures.

4.4. Pore fractal characteristics

According to the LTNA data and the FHH model, the fractal fitting curve of $\ln(V/V_0)$ vs $\ln(\ln(P_0/P))$ was obtained using Equation (1) (Fig. 7
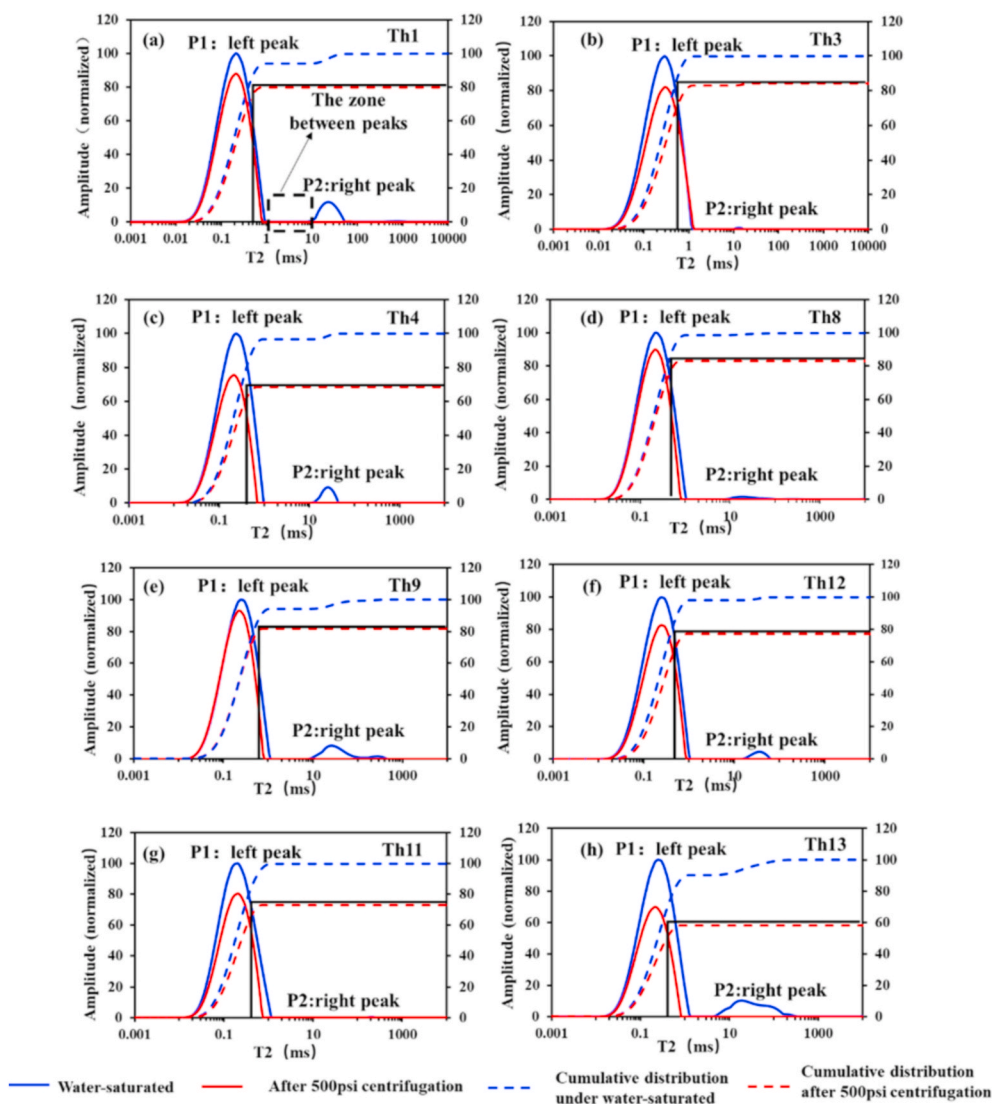

Fig. 6. NMR T_2 spectrum of the reservoirs before and after centrifugation, the T2 value of P1 ranges from 0.03 to 1 ms, the T2 value of P2 mainly ranges from 10 to 100 ms. (a) Th1, Type RI, bimodal pattern; (b) Th3, Type RIII, left unimodal pattern, the area of P2 is close to 0. (c) Th4, Type RIII, bimodal pattern; (d) Th8, Type RII, unimodal pattern; (e) Th9, Type RI, bimodal pattern; (f) Th12, Type RII, bimodal pattern; (g) Th11, Type RIII, left unimodal pattern, the area of P2 is close to 0; (h) Th13, Type RI, bimodal pattern, the wide P2 peak.

Table 5
Movable fluid parameters and fractal dimensions obtained from NMR.

Samples	Depth/m	Ps(%)	Sm(%)	Si(%)	Min (D_{NMR})	R_2	Max (D_{NMR})	R_2
Th1	3646.5	2.8	23.78	76.22	0.5344	0.867	2.9914	0.7700
Th3	3521.9	1.4	7.20	92.8	0.4506	0.8688	/	/
Th4	3524.3	2.9	35.85	64.15	0.1566	0.8593	2.9914	0.5368
Th8	3489.6	4.6	20.86	79.14	0.3666	0.8551	2.9977	0.6436
Th9	3825.2	4.5	25.87	74.13	0.2617	0.8531	2.991	0.8465
Th11	3526.8	1.2	6.95	93.05	0.1761	0.851	/	/
Th12	3489.4	5.9	23.42	76.58	0.2723	0.8516	2.997	0.7420
Th13	3504.4	2.4	45.26	54.74	0.5983	0.8664	2.9842	0.8493

Ps = porosity at 100% water saturation; Si = irreducible water saturation; Sm = moveable fluid saturation.

and Table 6). For all of the samples, the fractal fitting curves can be divided into two different linear segments at relative pressure (P/P₀) of 0–0.45 and 0.45–1.0, and P/P₀ = 0.45 corresponds to the point of the hysteresis loop closure. Additionally, every segment exhibits a good linear correlation ($R^2 > 0.965$), indicating that the two sections have different gas adsorption characteristics. Therefore, considering the difference in the gas adsorption behavior at P/P₀ > 0.45 and P/P₀ < 0.45, the fractal dimension of the sample should also be determined in two sections respectively and defined as D_1 (P/P₀ > 0.45) and D_2 (P/P₀ < 0.45) (Table 6). D_1 and D_2 correspond to the pore surface and pore space structural fractal dimensions, respectively (Li et al., 2019b). For the 14 tight reservoir samples from J_2q_2, all of the fractal dimension values are between 2 and 3, indicating that the pores of the mixed siliciclastic-carbonate rock reservoirs have a fractal geometry. The D_1 values vary from 2.4305 to 2.7081, with a mean of 2.5314; and the D_2 values vary from 2.2667 to 2.607, with a mean of 2.4491. The D_2 values are slightly lower than the D_1 values, suggesting the heterogeneity of the small pores is weaker than that of large pores (Wang et al., 2015). Moreover, D_1 is positively correlated with D_2 for the lacustrine mixed siliciclastic-carbonate sedimentary rocks (Table 6 and Fig. 13a), and the relationship is different from that for coals (Wang et al., 2015; Yao et al., 2008). The relationship shows that both D_1 and D_2 can be used to evaluate the heterogeneity of the pore structure of the organic-rich mixed siliciclastic-carbonate reservoirs.

The NMR fractal dimensions depend on the NMR T_2 relaxation time distribution. For the eight tight reservoir samples from J_2q_2, the NMR T_2 spectra exhibit bimodal patterns, and the peak P_1 is much higher than peak P_2, which suggests that the mesopores are dominant in the tight low maturity mixed siliciclastic-carbonate sedimentary rock reservoirs. According to the NMR fractal model, the fractal fitting curves of lg(V) vs lg(T_2) were obtained using Equation (4), and the fractal dimensions were calculated. As shown in Fig. 8 and Table 5, taking the T_2 cutoff value ($T_{2c} = 0.5$ ms) as the cut-off point, the fitting curve can be divided into two different linear segments. The fractal dimension of the linear part with T_2 value less than T_{2c} (0.5 ms) is defined as min(D_{NMR}), which mainly reflects the pore structure of the bound fluid. The fractal dimension of the linear part in which $T_2 > T_{2c}$ is defined as max(D_{NMR}), which reflects the pore structure of the movable fluid. The min(D_{NMR}) values range from 0.2617 to 0.5983, with an average of 0.4067. The max (D_{NMR}) values are greater than 2.99, which are close to 3, and the differences among all of the samples are very small, indicating that the macropores have a more complicated pore structure. However, the fractal dimensions of the bound fluid are less than 1, which exceeds the reasonable range of the fractal dimension. This result also suggests that the fractal dimensions of tight reservoirs containing a large amount of small pores or bound fluid cannot be reliably calculated using the NMR fractal method.

5. Discussion

5.1. Effects of mineralogical composition on pore structure

The pore structure results obtained from the N_2 adsorption

experiments reveal that pores are 2–100 nm in size, which is suitable for characterizing the mixed siliciclastic-carbonate reservoirs in the J_2q_2 (Li et al., 2020). The mineralogical compositions of the organic-rich tight mixed siliciclastic-carbonate reservoirs are complex, and they have an important effect on the pore structure of the tight reservoirs. The studied samples were deposited in a mixed siliciclastic-carbonate lacustrine sedimentary environment. The main components are carbonate, clay, quartz and feldspar, which are concomitant with the solid organic matter (Feng et al., 2019). As is shown in Fig. 9, for the same rock type, the effects of the clay, dolomite, silicate minerals and TOC contents on the BET SSA and TPV values are different. For different rock types, there are some relationships between some of these geological properties and pore structure parameters. There is a negative correlation between TOC content and the pore structure parameters. The BET SSA and TPV values decrease with increasing TOC content (Fig. 9a and b). This is possibly because, at higher TOC levels, the organic matter pores may collapse due to the relative weakened protection from mineral grains, thus producing more complex smaller pores. This correlation is different from that of continental shale oil reservoirs and marine shale gas reservoirs in other areas (Yang et al., 2016; Chen et al., 2019). However, it is similar to that of transitional shale gas reservoir in the Shanxi Formation in the Ordos Basin (Yang et al., 2017a, 2017b). This is probably because of the low-maturity of samples. Previous studies have shown that a large amount of OM pores appear in the solid OM only when the organic matter maturity (Ro) is greater than 1.1%. After which, as the total organic carbon content and the organic matter maturity increases, the volume and internal specific surface area of the organic matter pores grow. However, the content and maturity of the OM in the tight reservoirs of J_2q_2 are low-medium, and they are difficult to form a large number of OM pores under these conditions. In addition, the SEM observations revealed that the porosities of the organic matter were very poor, and only a few of marginal pores were observed between the OM and the mineral particles (Fig. 3h). Therefore, the differences in the organic matter maturity may account for the negative correlations between the TOC content and the pore structure parameters (Li et al., 2019b).

The dolomite content is positively correlated with the BET SSA and BJH TPV values, and the correlation with BJH TPV is significantly better than that with BET SSA (Fig. 9c and d). The correlations between the BET SSA, BJH TPV, and dolomite contents of Type RII and RIII are slightly higher than those for Type RI. However, there is a faint negative correlation between the pore structure parameters (SSA and TPV) and the calcite content (Fig. 9g and h). The relationships indicate that the dolomite in the tight reservoirs has a significant effect on the development of the pores. The higher dolomite contents correspond to larger amounts of micro-scale pores and larger pore volumes. The reason for this is that large amounts of dolomite interparticle pores were formed by the dolomitization. The dolomite also forms a rigid framework increasing the compressive strength of the tight reservoirs, which is conducive to the preservation of small pores. The clay content is positively correlated with BET SSA, and the correlation of Type RI is much stronger than the other rock types. However, there is no obvious correlation between the clay content and BJH TPV. These relationships
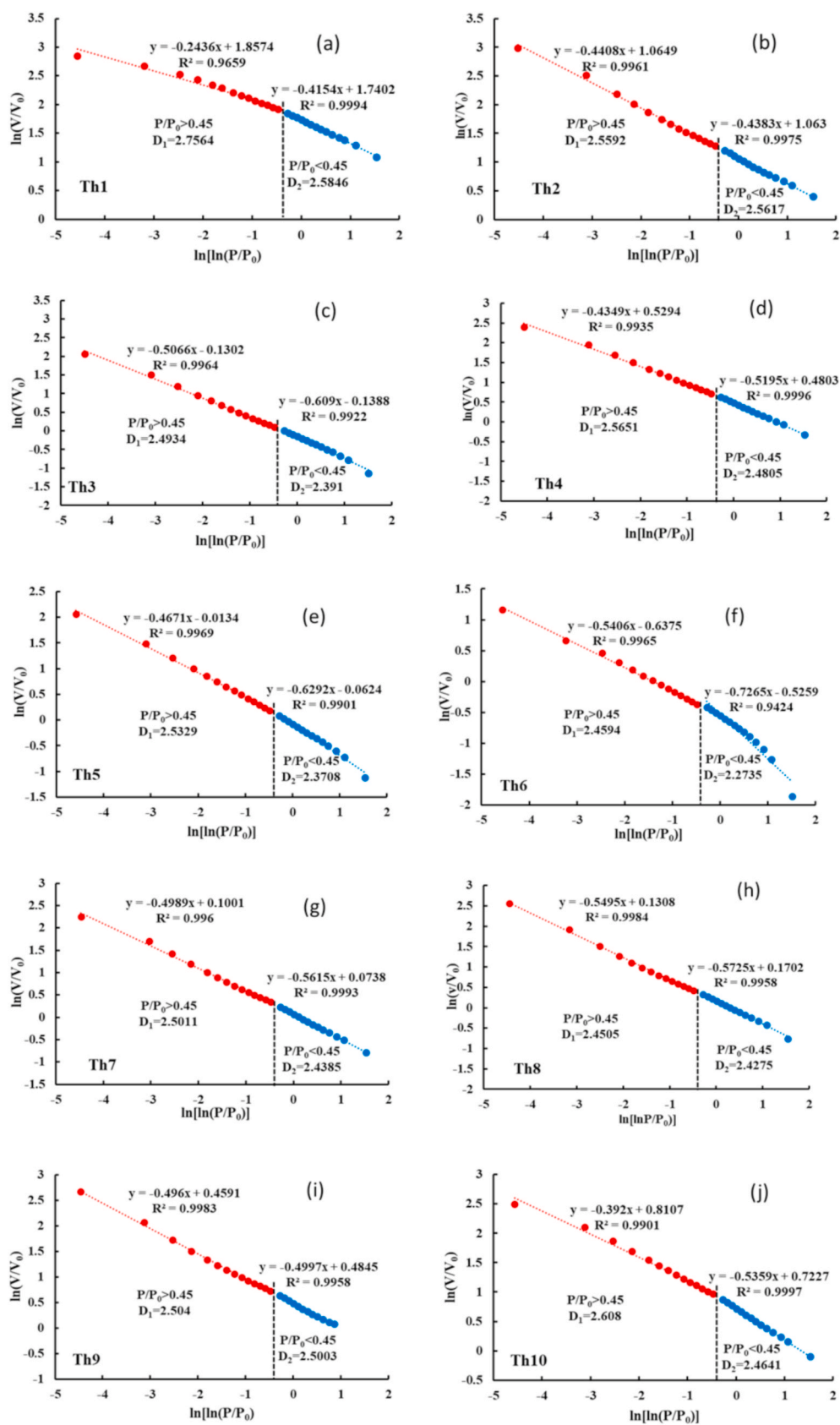
Fig. 7. Crossplots of $\ln(V/V_0)$ vs $\ln(\ln(P/P_0))$ obtained from N_2 adsorption data for tight reservoir samples. (a) Sample Th1, $D_1 = 2.7564$, $D_2 = 2.5846$; (b) Sample Th2, $D_1 = 2.5592$, $D_2 = 2.5617$; (c) Sample Th3, $D_1 = 2.4934$, $D_2 = 2.3910$; (d) Sample Th4, $D_1 = 2.5651$, $D_2 = 2.4805$; (e) Sample Th5, $D_1 = 2.5329$, $D_2 = 2.3708$; (f) Sample Th6, $D_1 = 2.4594$, $D_2 = 2.2735$; (g) Sample Th7, $D_1 = 2.5001$, $D_2 = 2.4385$; (h) Sample Th8, $D_1 = 2.4505$, $D_2 = 2.4275$; (i) Sample Th9, $D_1 = 2.5040$, $D_2 = 2.5003$; (j) Sample Th10, $D_1 = 2.6080$, $D_2 = 2.4641$; (k) Sample Th11, $D_1 = 2.5295$, $D_2 = 2.4374$; (l) Sample Th12, $D_1 = 2.4928$, $D_2 = 2.4873$; (m) Sample Th13, $D_1 = 2.7108$, $D_2 = 2.607$; (n) Sample Th14, $D_1 = 2.4305$, $D_2 = 2.2667$.
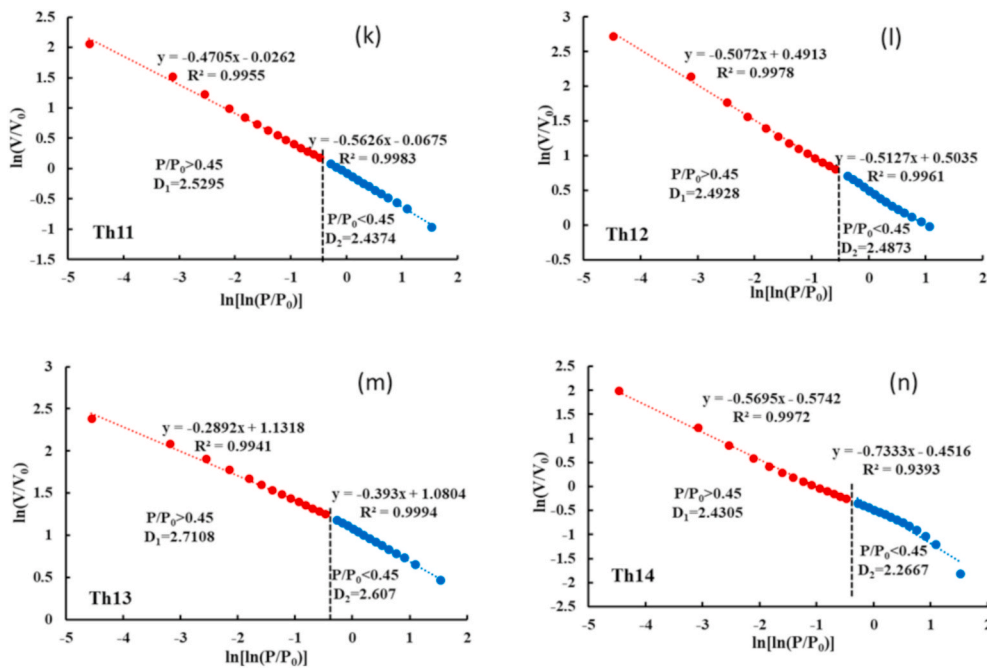
Fig. 7. (*continued*).

Table 6
Fractal dimensions derived from Frenkel-Halsey-Hill model.

Sample ID	Depth(m)	P/P_0:0.45–1.0				P/P_0:0–0.45			
		Fractal fitting equation	A_1	$D_1 = 3 + A_1$	R^2	Fractal fitting equation	A_2	$D_2 = 3 + A_2$	R^2
Th1	3646.5	$-0.2436X+1.8574$	-0.2436	2.7564	0.9659	$-0.4154X+1.7402$	-0.4154	2.5846	0.9994
Th2	3486.2	$-0.4383X+1.063$	-0.4383	2.5617	0.9985	$-0.4408X+1.0649$	-0.4408	2.5592	0.9985
Th3	3521.9	$-0.5066X+0.1302$	-0.5066	2.4934	0.9964	$-0.609X+0.1388$	-0.609	2.3910	0.9922
Th4	3524.3	$-0.4349X+0.5294$	-0.4349	2.5651	0.9935	$-0.5195X+0.4803$	-0.5195	2.4805	0.9996
Th5	3852.0	$-0.4671X-0.0134$	-0.4671	2.5329	0.9969	$-0.6292X-0.0624$	-0.6292	2.3708	0.9424
Th6	3863.9	$-0.5406X+0.6375$	-0.5406	2.4594	0.9965	$-0.7265X+0.5259$	-0.7265	2.2735	0.983
Th7	3889.8	$-0.4989X+0.1001$	-0.4989	2.5011	0.9956	$-0.5615X+0.0738$	-0.5615	2.4385	0.9993
Th8	3489.6	$-0.5495X+0.1308$	-0.5495	2.4505	0.9984	$-0.5725X+0.1702$	-0.5725	2.4275	0.9958
Th9	3825.2	$-0.496X+0.4591$	-0.4960	2.5040	0.9983	$-0.4997X+0.4845$	-0.4997	2.5003	0.9958
Th10	3887.9	$-0.392X+0.8107$	-0.3920	2.6080	0.9901	$-0.5359X+0.7227$	-0.5359	2.4641	0.9997
Th11	3526.8	$-0.4705X-0.0262$	-0.4705	2.5295	0.9955	$-0.5626X-0.0675$	-0.5626	2.4374	0.9983
Th12	3489.4	$-0.5072X+0.4913$	-0.5072	2.4928	0.9978	$-0.5127X+0.5035$	-0.5127	2.4873	0.9961
Th13	3504.4	$-0.2892X+1.1318$	-0.2892	2.7108	0.9941	$-0.393X+1.0804$	-0.393	2.6070	0.9994
Th14	3510.7	$-0.5695X-0.5742$	-0.5695	2.4305	0.9972	$-0.7333X-0.4516$	-0.7333	2.2667	0.9393

Note: A is the slope of Equation (1); R^2, correlation coefficients; D_1 and D_2 means fractal dimension D from Equation (3).

indicate that the clay minerals contribute great to the pore surface area, and which also have the ability to bind pore fluids. Moreover, the SEM observations revealed that the plate-shaped clay minerals fill the inter-particle pores, which results in a more complex pore structure. As shown in Fig. 9i and j, for Type RI, the BET SSA and BJH TPV values decrease slightly with increasing silicate mineral content, whereas there are no clear relationships between the pore structure parameters and the silicate mineral content for Types RII and RIII. These results suggest that the tiny silicate grains contribute little to the development of pores.

In fine-grained mixed siliciclastic-carbonate sedimentary environments, an increase in the quartz and feldspar content reflects an increased supply of terrigenous materials, which is not favorable to the formation of rigid calcareous (Li et al., 2017). However, carbonate minerals tend to develop more interparticle pores, such as the large number of dolomites interparticle pores formed by the dolomitization during the burial diagenesis, which is an important reason for the formation of intergranular pores in carbonate reservoirs. When one Ca^{2+} of two $CaCO_3$ molecules is replaced by Mg^{2+}, the volume is reduced and the intercrystalline pore is formed due to the fact that the Mg^{2+} radius (0.078 nm) is smaller than that of Ca^{2+} (0.106 nm). According to the

theoretical calculation, the volume of 1 mol calcite is about 36.8cm3, and the volume of 1 mol dolomite is about 64.5cm3. In the process of dolomization, while 2 mol calcite transformed into 1 mol dolomite (1molCa^{2+} was replaced by Mg^{2+}), the volume is decreased by 9.1 cm3, which accounts for 12.39% of the total volume of 2 mol calcite. If the contents of Mg^{2+} is insufficient, the dolomization is not complete, or mixed with other ions(Fe^{2+}), resulting in a smaller volume of inter-crystalline pore shrinkage than 9.12cm3, according to statistics, if calcite is completely replaced by dolomite, the reservoirs porosity could increase to 12 %–13% (Li et al., 2020). The correlations between the silicate minerals content and the pore structure parameters are similar to the research results for Chang 7 shale oil reservoir in the Upper Triassic in the Ordos Basin (Liu et al., 2015; Yang et al., 2016), but they are opposite to the results of previous studies of the Wufeng-Longmaxi in the Sichuan Basin and the Devonian shale gas reservoirs in northeastern British Columbia, Canada (Yang et al., 2014, 2017a, 2017b). Distinct relationships in different areas are related to the origin of siliceous mineral and depositional environments (Chalmers et al., 2012; Yang et al., 2017a, 2017b; Li et al., 2019b). The Chang 7 shales in the Yanchang Formation and the organic-rich mixed siliciclastic-carbonate
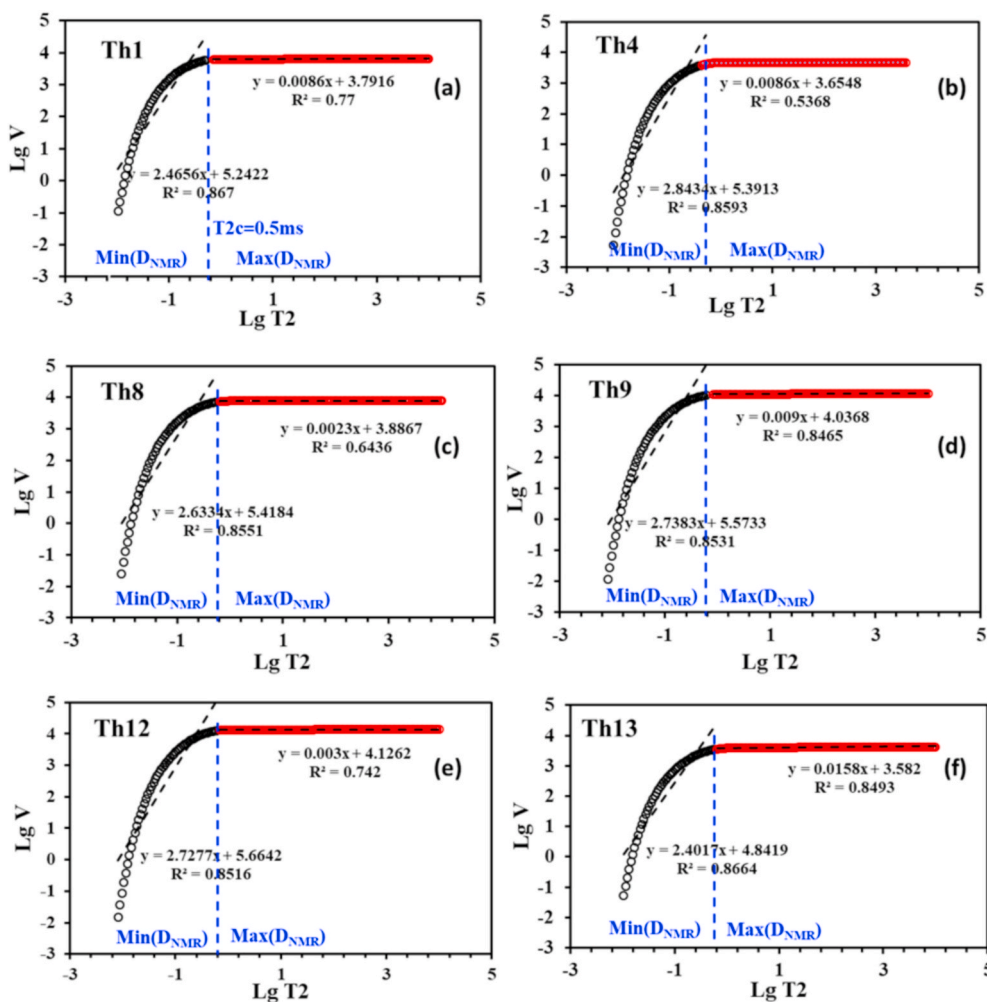
Fig. 8. The fractal curves of NMR from some samples. (a) Fitting curves of sample Th1; (b) Fitting curves of sample Th4; (c) Fitting curves of sample Th8; (d) Fitting curves of sample Th9; (e) Fitting curves of sample Th12; (f) Fitting curves of sample Th13.

rocks in J_2q_2 were deposited in lacustrine environments and siliceous minerals mainly are from terrigenous clastics. However, the marine shale in the Sichuan Basin and the Devonian shale in British Columbia were deposited in deep-water shelf sedimentary environments where biogenic siliceous minerals are dominant (Wang et al., 2014).

The percentages of the movable fluids (Sm) obtained from the NMR investigation of the samples after centrifugation can be effectively used to characterize the heterogeneity of the pore structure effectively. As is shown in Table 5, the movable fluid saturation varies from 6.95% to 45.62%, with a mean of 23.02%. The effects of clay mineral, siliceous mineral, and dolomite content on the mobile fluid saturation are illustrated in Fig. 10. The mobile fluid saturation is positively correlated with the dolomite content, but it is poorly correlated with the siliceous mineral and clay mineral contents. This suggests that the pores holding movable fluid are mainly dolomite interparticle pores (Fig. 10a and b). The fact that sample (Th13) differs from the other samples (black circle) is ascribed to the presence of well-developed micro-fractures (Fig. 10). However, the clay and siliceous minerals forming the nanoscale interparticle pores are poor and disconnected, and thus, they are not conducive to fluid flow. In addition, dolomite interparticle pores were also observed using SEM. They have significantly better pore size and connectivity than the other types of pores. The above consistent results demonstrate that both the N_2 adsorption and NMR methods can be used to evaluate the pore structure characteristics of the mixed siliciclastic-carbonate sedimentary rock reservoirs in J_2q_2.

5.2. Correlation between pore distribution and sedimentary texture

According to the results presented in Section 4.1, the J_2q_2 organic-rich mixed siliciclastic-carbonate sedimentary rocks include three rock types with different sedimentary texture. The pore sizes and pore distributions of these different sedimentary texture types are different. According to the distribution of the NMR T_2 spectrum under water-saturated conditions (Fig. 6), all of the samples have similar distributions of $T_2 < 1$ ms. The T_2 spectra of Type RI and Type RII exhibit patterns with a high peak P_1 and a low peak P_2, whereas the T_2 spectra of Rock Type III exhibit left unimodal patterns. In addition, the NMR porosities of Type RI and Type RII (2.4%–4.5% and 4.6%–5.9%, respectively) are significantly higher than those of Rock Type III (1.2%–2.9%) (Fig. 11a). The pore size and pore morphology characteristics are illustrated in Figs. 4, 5 and 11b. Most of Type RI and Type RII exhibit bimodal patterns, and their average pore diameters (APD) range from 7.63 to 23.59 nm with an average of 16.79 nm and 17.57–21.81 nm with an average of 19.69 nm. However, Type RIII has a wide range of APD, which may be related to the mineral particle size and organic matter content. According to the shapes of the hysteresis loops, the pore shapes of Type RII are mainly slit-shaped pores, whereas those of Type RI are a mixture of slit-shaped and the ink-bottle pores. Most of Type RIII exhibit unimodal pattern, the APD values vary from 7.99 to 18.37 nm with an average of 14.46 nm, and their pores are mainly ink-bottle-shaped. The above results suggest that the pore sizes of the rocks with a large amount of intraclasts and massive textures are slightly higher than the rock with
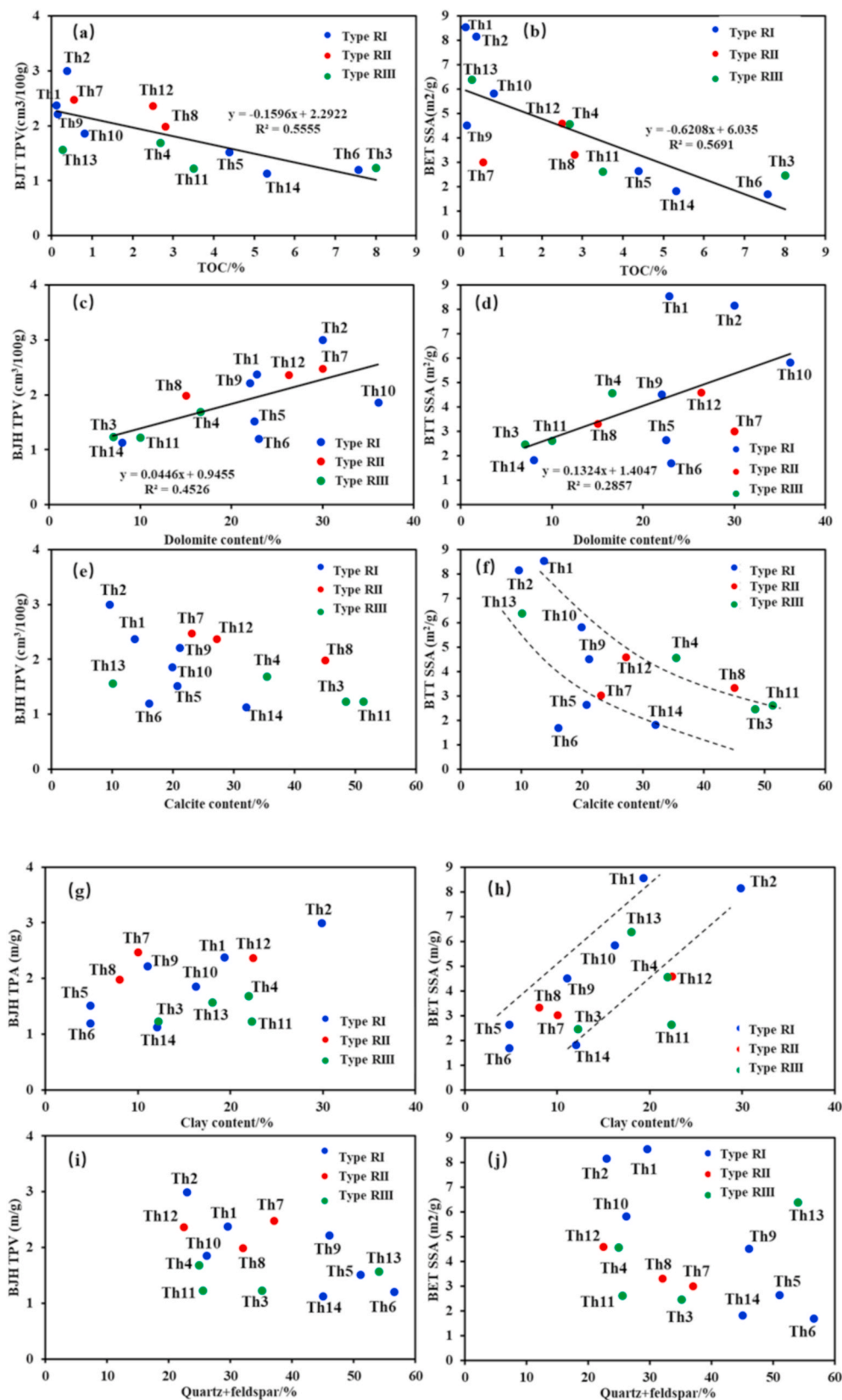
Fig. 9. The Correlations between TOC values, dolomite, calcite, clay mineral, quartz + feldspar and BJH TPV and BET SSA measured by N$_2$ adsorption, respectively.
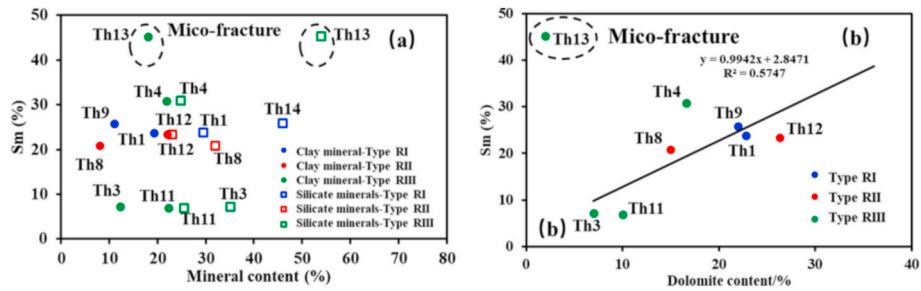
Fig. 10. (a) Relationships between the clay minerals, silicate minerals and movable fluid parameters (Sm). (b) Relationship between dolomite and movable fluid saturation (Sm).
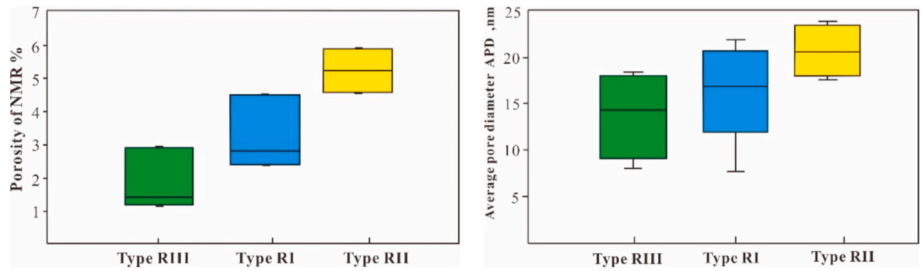

Fig. 11. (a) The comparison of the NMR porosity from different rock types with different sedimentary textures; (b) The comparison of average pore diameter value obtained from low-temperature N2 adsorption of different rock types with different sedimentary textures.

laminated textures. Differences in diagenetic and depositional environments may explain these results. Rocks with a large amount of intraclasts and massive sedimentary textures (Types RI and RII) deposited in the shallow-water environments, which is conducive to the development of rigid carbonate minerals, so they are prone to interparticle porosity. Moreover, a turbulent water column makes it difficult for the fine-grained components (argillaceous) and organic matter to fill the interparticle pores between the rigid mineral. In addition, the primarily preserved interparticle pores are favorable to the flow of diagenetic fluids, which may form dolomite interparticle pores due to the dolomitization during the burial diagenesis. However, the rocks with laminated textures (Type RIII) are usually rich in organic matter and were deposited in a deep-water sedimentary environment with significantly stratified conditions (Zhang et al., 2018). The fine-grained components and organic matter were frequently interbedded with carbonate, which are not favorable to the development of OM pores and dissolution pores in the low-maturity stage (Yang et al., 2017a, 2017b; Liang et al., 2019). In addition, due to the influence of burial compaction, it is often difficult for the fine-grained components to form larger interparticle pores. However, the dense packing of the larger particles tends to form relatively uniform, larger pores (Liang et al., 2019).

5.3. Comparison of the fractal dimensions from the LTNA and NMR data

In this study, the LTNA and NMR methods were used to calculate the fractal dimensions of the pore structures, and the results are shown in Fig. 12. The NMR T_2 spectrum distribution under water-saturated conditions shows that the left peak ($T_2 < 1$ ms) has a relatively high percentage. This corresponds an approximate pore size range of 2–100 nm, accounting for more than 80%, which was calculated using the conversion coefficient $C = 20$ (Li et al., 2020). Based on the fractal theory of pore structures and its applicable conditions, the fractal dimension value is usually between 2 and 3 (Jaroniec et al., 1995). However, the NMR fractal dimensions corresponding to the smaller pores ($r < 50$ nm) in the samples from J_2q_2 are all less than 1. Additionally, the fractal dimensions corresponding to the larger pores are all greater than 2.99, which is close to 3 and do not show any differences. This result is not
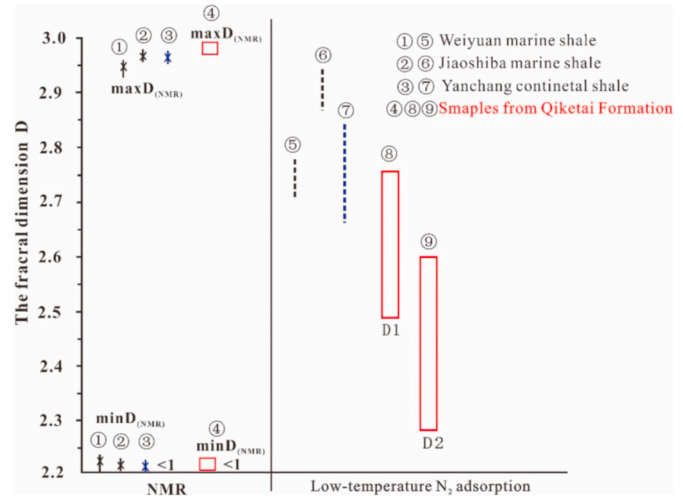

Fig. 12. The fractal dimension comparison of the fine-grain sedimentary rocks in different areas using different methods (the additional data from Liu et al. (2015), Li et al. (2018) and Yang et al., 2017a, 2017b).

consistent with the fractal theory of pore structures and the applicable conditions of the fractal dimension calculation. Therefore, the pore fractal dimensions of the mixed siliciclastic-carbonate sedimentary rock reservoirs with NMR T_2 spectra containing a higher P_1 peak and an extremely low P_2 peak cannot be evaluated using NMR fractal method. The N_2 adsorption experiment can effectively characterize the differences in the pore structures and fractal characteristics of tight reservoirs with pore sizes of 2–100 nm (Yang et al., 2017a, 2017b), which matches the major pore size distribution range of the organic-rich mixed siliciclastic-carbonate reservoirs investigated in this study. Therefore, the fractal dimension obtained from the N_2 adsorption data is between 2 and 3, which is consistent with the applicable conditions of the pore fractal dimension calculations and can reflect the pore structure heterogeneity of the mesopores (2–50 nm). These results are consistent with
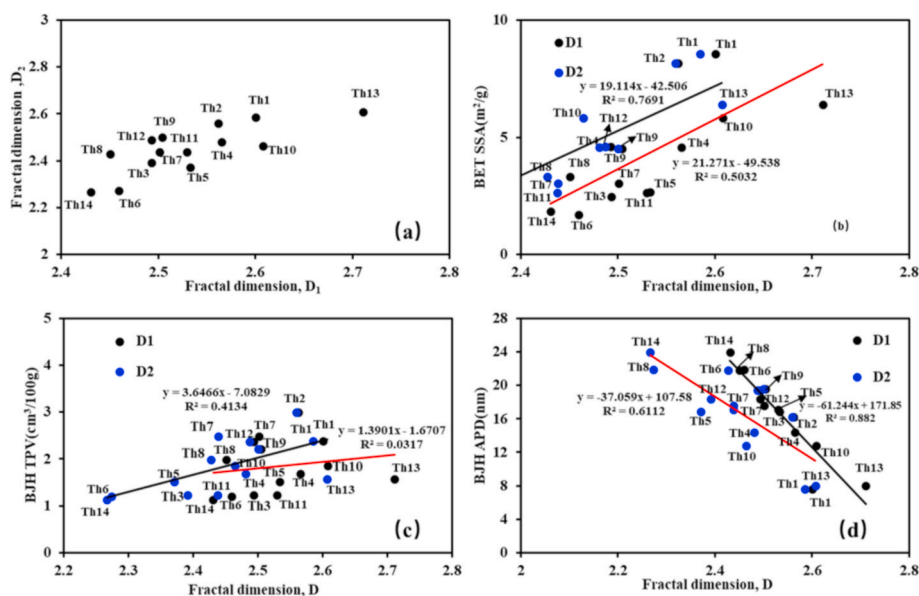
Fig. 13. Relationship between fractal dimension and pore structural parameters. (a) The plot of Fractal dimension D_2 versus Fractal dimension D_1; (b) The plots of BET specific surface areas (SSA) versus fractal dimension D; (c) The plot of BJH total pore volume (TPV) versus fractal dimension D; (d) BJH average pore diameter (APD) versus fractal dimension D.

the results of the fractal dimensions obtained for the marine shale gas reservoirs in the Longmaxi Formation in the Jiaoshiba and Weiyuan areas in the Sichuan Basin and the Chang 7 lacustrine shale oil reservoirs in the Ordos Basin (Liu et al., 2015; Li et al., 2018, Fig. 12). The NMR fractal dimensions of the smaller pores are less than 2, which is outside of the reasonable range of fractal dimension values. Moreover, the fractal dimensions of the larger pores are close to 3, which makes it difficult to effectively characterize the change in the pore complexity. In contrast, low temperature N_2 adsorption experiments have some advantages in the characterization of the fractal dimensions of smaller pores (Li et al., 2019b; Yang et al., 2017a, 2017b). The above research shows that the pore structure of the tight reservoirs in the study area can be characterized using NMR method, but it is not the best method to evaluate the fractal characteristics of the pores. The main reason for this is that the two methods have different pore measurement ranges. The above analysis results show that the pore structure parameters obtained from the N_2 adsorption effectively reflect the fractal characteristics of the nanoscale pores (r = 2–50 nm) in the studied samples.

5.4. Pore structure parameters and fractal dimensions

As shown in Fig. 13, the fractal dimensions (D_1 and D_2) are positively correlated with BET SSA (Fig. 13b). The correlation ($R^2 = 0.7691$) between D_2 and BET SSA is much stronger than that between D_1 and the BET SSA ($R^2 = 0.5032$), indicating that D_2 may represent the heterogeneity of the pore specific surface area better. The slightly positive correlations between BJH TPV and the fractal dimensions (Fig. 13c), suggest that BJH TPV has a little influence on fractal dimensions. However, the correlations between BJH TPV and the fractal dimensions are significantly lower than those between BET SSA and the fractal dimensions. The reason for this may be that the organic-rich mixed siliciclastic-carbonate sediments are composed of tiny particles, and the particle size and the accumulation state are apt to influence the specific surface area and pore volume, especially the latter (Cai et al., 2013; Yang et al., 2014). The upper limit of the fractal dimension is far less than the diameter of the particles, and the accumulation shape of the particles should not affect the fractal dimension (Cai et al., 2013). The APD values of the tight reservoirs exhibit sharp negative correlations with the fractal dimensions (D_1 and D_2), and the fractal dimension decrease with increasing APD (Fig. 13d). These results show that the

pore structure of the larger pores is more complex than smaller pores within the range of the mesopores. The correlation between D_1 and APD is stronger than that between APD and D_2, indicating that D_1 may be a good parameter for representing the irregularity and roughness of the pore space structure. The above analysis shows that the organic-rich tight reservoirs have medium-high fractal dimensions. Therefore, the larger the value of D_1 is, the more irregular the pore surface and the larger of the SSA will be. The larger the value of D_2 is, the more irregular the pore structure is, and the smaller the APD will be.

5.5. Correlations between the fractal dimensions and TOC content, mineralogical composition

To investigate the influence of the main mineralogical compositions and TOC content on the pore fractal dimensions of the organic-rich mixed siliciclastic-carbonate reservoirs, the related plots are illustrated in Fig. 14. The D_1 values slightly decrease with increasing TOC content (Fig. 14a), whereas there is no clear relationship between D_2 and TOC content, indicating that the OM content has a little negative impact on D_1. The possible reason for this is that the OM pores within the solid organic matter are poorly developed, whereas the regular and elongated grain-edged pores between the rigid minerals and the solid organic matter are slightly developed. These pores were observed under the SEM, and they may be residual interparticle pores filled with solid organic matter, which suggests that the OM contributes little to the BET SSA and BJH TPV. The grain-edged pores are also slightly larger in size and have relatively regular pore structures with smooth, and straight pore wall. However, this type of pore is not predominant in the studied samples, and thus, these pores have little effect on the irregularity of the pore space structure (Yang et al., 2017a, 2017b; Li et al., 2019b). The dolomite content exhibits a clear positive correlation with the fractal dimension D_1 (Fig. 14b), while there is a positive correlation between the clay mineral content and the fractal dimension D_2 (Fig. 14c). These correlations suggest that increases in the dolomite and clay mineral contents lead to more complicated and irregular pore structures. In summary, the clay minerals mainly affect the irregularity of the pore specific surface area, while dolomite mainly affects the irregularity of the pore space structure. It is possible that the fine-grained reservoir samples with higher clay contents contain more absorbed water and have more small pores. The pores are more irregular and heterogeneous
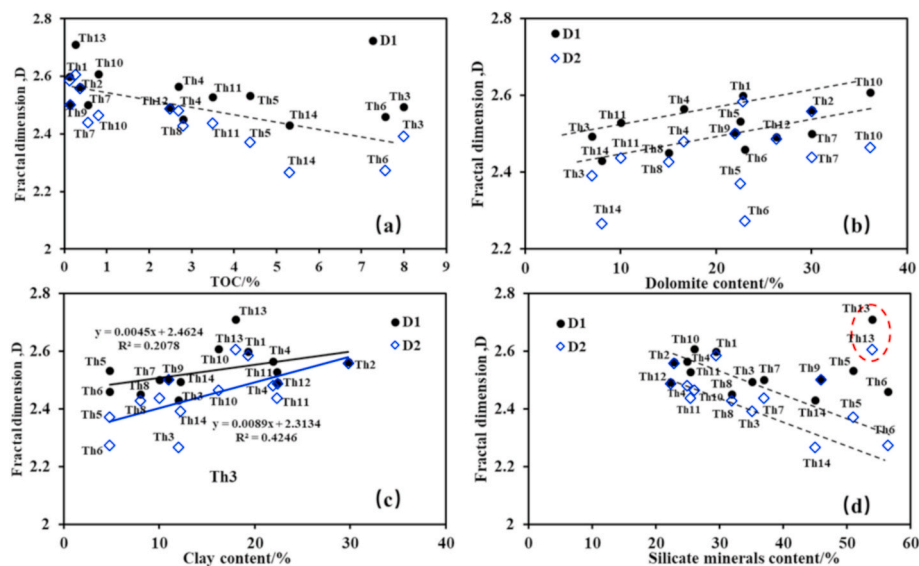
Fig. 14. Relationship between fractal dimension and TOC (a), dolomite content (b), clay content (c) and silicate minerals content (d).

as a result of the smaller micro-pore volume, capillarity and the filling of water molecules (Li et al., 2017). In addition, at high clay levels, the primary interparticle pores may collapse due to the relative weakened protection from rigid mineral grains, thus producing more complex smaller pores. The samples with high dolomite contents generally contain large amounts of dolomite intercrystalline pores, and meanwhile, the dolomitization and the associated weak dissolution make pore morphology irregular during the burial diagenesis (Li et al., 2019b, 2020). Therefore, the large amounts of irregular dolomite intercrystalline pores would increase the fractal dimension D_1 in the tight reservoirs. There is also a slight negative correlation between fractal dimensions (D_1 and D_2) and the silicate minerals (quartz and feldspar) content, indicating that quartz and feldspar have a little influence on the pore space structures and surface (Fig. 14d). However, sample Th13, which has a high silicate minerals content, has a higher fractal dimension than the other samples (red dotted circle). This may be related to the presence of micro-fractures in this sample, which would increase the complexity and irregularity of the pore structure. Under the fine-grained mixed siliciclastic-carbonate sedimentary environment, the input of terrigenous clastics is not conducive to the development of micropores, and it can even fill the intercrystalline pores. Therefore, silicate minerals decrease the pore volume, specific surface area, and fractal dimensions of pore structure in the tight reservoirs.

6. Conclusions

(1) The organic-rich mixed siliciclastic-carbonate tight rocks investigated in this study can be divided into three types of lithofacies: massive silt-bearing argillaceous micritic dolomite (Type RI), silt-bearing calcitic dolomite with a large amount of intraclasts (Type RII), and laminated silt-bearing argillaceous micritic limestone (Type RIII). The pores developed in mixed sedimentary siliciclastic-carbonate rocks are mainly interparticle pores between particles and crystals. The OM pores are poorly developed. The small pores (2–100 nm) make a significant contribution to the nanoscale pore spaces in the samples.

(2) The pore shapes are mainly slit-shaped, followed by ink-bottle shaped and mixed type. The BJH TPV and APD values of Type RII are slightly higher than those of Types RI and RIII. Based on the low temperature N_2 adsorption data, most of the mesopores are around the major peak at 2–4 nm, but some of the pores are distributed around the major peak at 6–35 nm.

(3) The massive and intraclasts-rich mixed siliciclastic-carbonate reservoirs have higher NMR porosities and pore sizes than those of the rocks with laminated textures. The low temperature N_2 adsorption method can effectively characterize the pore structure fractal characteristics of mixed siliciclastic-carbonate reservoirs with pore sizes of 2–100 nm.

(4) In the mixed siliciclastic-carbonate sedimentary rocks, the dolomite contributes more significantly to the pore volume and movable fluid than the silicate minerals and organic matter, resulting in higher fractal dimensions and more irregular pore structures. In addition, the clay minerals increase pore specific surface area and complexity of the tight reservoirs. Samples with high TOC contents and silicate mineral contents have low pore specific surface area, low pore volume and fractal dimensions.

Author contribution

Tianjun Li: Experiments, Software, Investigation, Writing – original draft. Zhilong Huang: Conceptualization, Methodology. Jing Zhao: Samples, Writing, Review & Editing. Xiongfei Xu: Review & Editing. Xiaobo Guo: Review & Editing; With kind regards, Zhilong Huang

Declaration of competing interest

The authors declare that they have no known competing financial interests or personal relationships that could have appeared to influence the work reported in this paper.

Acknowledgments

References

Avnir, D., Jaroniec, M., 1989. An isotherm equation for adsorption on fractal surfaces of heterogeneous porous materials. Langmuir 5, 1412–1433.
Bai, B., Zhu, R., Wu, S., Cui, J., Sun, L., Li, T., et al., 2014. New micro-throat structural characterization techniques for unconventional tight hydrocarbon reservoir. China Petroleum Exploration 19, 78–86.

Barrett, E.P., Joyner, L.G., Halenda, P.P., 1951. The determination of pore volume and area distributions in porous substances. I. Computations from nitrogen isotherms. J. Am. Chem. Soc. 73 (1), 373–380.

Brunauer, S., Emmett, P.H., Teller, E., 1938. Adsorption of gases in multimolecular layers. J. Am. Chem. Soc. 60 (2), 309–319.

Burton, Z.F.M., Moldowan, J.M., Sykes, R., Graham, S.A., 2018. Unraveling petroleum degradation, maturity, and mixing and addressing impact on petroleum prospectivity: insights from frontier exploration regions in New Zealand. Energy Fuel. 32 (2), 1287–1296.

Burton, Z.F.M., Moldowan, J.M., Magoon, L.B., Sykes, R., S A, 2019. Graham. Interpretation of source rock depositional environment and age from seep oil, east coast of New Zealand. Int. J. Earth Sci. 108 (4), 1079–1091.

Cai, Y., Liu, D., Pan, Z., Yao, Y., Li, J., Qiu, Y., 2013. Pore structure and its impact on CH4 adsorption capacity and flow capability of bituminous and subbituminous coals from Northeast China. Fuel 103, 258–268.

Chalmers, G.R.L., Bustin, R.M., Power, I.M., 2012. Characterization of gas shale pore systems by porosimetry, pycnometry, surface area, and field emission scanning electron microscopy/transmission electron microscopy image analyses: examples from the Barnett, Woodford, Haynesville, Marcellus, and Doig units. AAPG Bull. 96 (6), 1099–1119.

Chen, K., Liu, X., Liu, J., Zhang, C., Guan, M., Zhou, S., 2019. Lithofacies and pore characterization of continental shale in the second member of the kongdian Formation in the Cangdong sag, Bohai Bay Basin, China. J. Petrol. Sci. Eng. 177, 154–166.

Chung, F.H., 1974a. Quantitative interpretation of X-ray diffraction patterns of mixtures. I. Matrix-flushing method for quantitative multicomponent analysis. J. Appl. Crystallogr. 7, 519–525.

Chung, F.H., 1974b. Quantitative interpretation of X-ray diffraction patterns of mixtures. II. Adiabatic principle of X-ray diffraction analysis of mixtures. J. Appl. Crystallogr. 7, 526–531.

Clarkson, C.R., Solano, N., Bustin, R.M., Bustin, A.M.M., Chalmers, G.R.L., He, L., 2013. Pore structure characterization of North American shale gas reservoirs using USANS/SANS, gas adsorption, and mercury intrusion. Fuel 103, 606–616.

Coffey, B.P., Read, J.F., 2004. Mixed carbonate-siliciclastic sequence stratigraphy of a Paleogene transition zone continental shelf, southeastern USA. Sediment. Geol. 166, 21–57.

Curtis, M.E., Sondergeld, D.H., Ambrose, R.J., 2012. Microstructural investigation of gas shales in two and three dimensions using nanometer-scale resolution imaging. AAPG (Am. Assoc. Pet. Geol.) Bull. 96, 665–677.

Dahl, J.E., Moldowan, J.M., Peters, K.E., Claypool, G.E., Rooney, M.A., Michael, G.E., Mello, M.R., Kohnen, M.L., 1999. Diamondoid hydrocarbons as indicators of natural oil cracking. Nature 399 (6731), 54–57.

Feng, J., Cao, J., Hu, K., Chen, Y., Yang, S., Liu, Y., Bian, L., Zhang, G., 2011. Forming mechanism of middle-deep mixed rock reservoir in the Qaidam basin. Acta petrologica 27 (8), 2461–2472.

Feng, Y., Huang, Z., Zhang, H., Wang, J., Peng, Y., 2019. Diamictite tight reservoir characterization of Qiketai Formation member-2 in the Shengbei depression of Tuha basin. Special Oil Gas Reservoirs 26, 56–63.

Gregg, S.J., Sing, K.S.W., 1982. Adsorption, Surface Area and Porosity, second ed. Academic Press, New York.

Guo, X.B., Huang, Z.L., Ding, X.J., Chen, J.L., Chen, X., Wang, R., 2018. Characterization of continental coal-bearing shale and shale gas potential in Taibei sag of the Turpan-Hami Basin, NW China. Energy Fuel. 32, 9055–9069.

Hantschel, T., Kauerauf, A.I., 2009. Fundamentals of Basin and Petroleum Systems Modeling. Springer.

Hu, S., Zhu, R., Wu, S., Bai, B., Yang, Z., Cui, J., 2018. Exploration and development of continental tight oil in China. Petrol. Explor. Dev. 45 (4), 790–802.

Huang, Z., Liu, G., Li, T., Li, Y., Yin, Y., Wang, L., 2017. Characterization and control of mesopore structural heterogeneity for low thermal maturity shale: a case study of Yanchang Formation shale, Ordos Basin. Energy Fuel. 31 (11), 11569–11586.

Jarvie, D.M., Hill, R.J., Ruble, T.E., Pollastro, R.M., 2007. Unconventional shale-gas systems: the Mississippian Barnett shale of north-central Texas as one model for thermogenic shale-gas assessment. AAPG Bull. 91 (4), 475–499.

Jaroniec, M., 1995. Evaluation of the fractal dimension from a single adsorption isotherm. Langmuir 11, 2316–2317.

Jiang, F., Chen, D., Wang, Z., Xu, Z., Chen, J., Liu, L., Huyan, Y., Liu, Y., 2016. Pore characteristic analysis of a lacustrine shale: a case study in the Ordos Basin, NW China. Mar. Petrol. Geol. 73, 554–571.

Komatsu, T., Naruse, H., Shigeta, Y., Takashima, R., Maekawa, T., Dang, H.T., Dinh, T.C., Nguyen, P.D., Nguyen, H.H., Tanaka, G., Sone, M., 2014. Lower Triassic mixed carbonate and siliciclastic setting with Smithian–Spathian anoxic to dysoxic facies, an Chau basin, northeastern Vietnam. Sediment. Geol. 300, 28–48.

Lai, J., Wang, G., Wang, Z., Chen, J., Pang, X., Wang, S., Zhou, Z., He, Z., Qin, Z., Fan, X., 2018. A review on pore structure characterization in tight sandstones. Earth Sci. Rev. 177, 436–457.

Li, J., Lu, S., Chen, G., Wang, M., Tian, S., Guo, Z., 2019a. A new method for measuring shale porosity with low-field nuclear magnetic resonance considering non-fluid signals. Mar. Petrol. Geol. 102, 535–543.

Li, T., Jiang, Z., Li, Z., Wang, P., Xu, C., Liu, G., Su, S., Ning, C., 2017. Continental shale pore structure characteristics and their controlling factors: a case study from the lower third member of the Shahejie Formation, Zhanhua Sag, Eastern China. J. Nat. Gas Sci. Eng. 45, 670–692.

Li, T., Huang, Z., Feng, Y., Chen, X., Ma, Q., Liu, B., Guo, X.B., 2020. Reservoir characteristics and evaluation of fluid mobility in organic-rich mixed siliciclastic-carbonate sediments: a case study of the lacustrine Qiketai Formation in Shengbei Sag, Turpan-Hami Basin, Northwest China. J. Petrol. Sci. Eng. 185, 106667.

Li, Y., Wang, Z., Pan, Z., Niu, X., Yu, Y., Meng, S., 2019b. Pore structure and its fractal dimensions of transitional shale: a cross-section from east margin of the Ordos Basin, China. Fuel 241, 417–431.

Li, Z., Shen, X., Qi, Z., Hu, R., 2018. Study on the pore structure and fractal characteristics of marine and continental shale based on mercury porosimetry, N2 adsorption and NMR methods. J. Nat. Gas Sci. Eng. 53, 12–21.

Liang, X., Chen, K., Zhang, T., Zhang, C., Zhang, J., Su, H., 2019. The controlling factors of depositional environment to pores of the shales:Case study of Wufeng Formation-Lower Longmaxi Formation in Dianqianbei area. Natural Gas Geoscience 30 (10), 1393–1405.

Liu, B., Bai, L., Chi, Y., Jia, R., Fu, X., Yang, L., 2019a. Geochemical characterization and quantitative evaluation of shale oil reservoir by two-dimensional nuclear magnetic resonance and quantitative grain fluorescence on extract: a case study from the Qingshankou Formation in Southern Songliao Basin, northeast China. Mar. Petrol. Geol. 109, 561–573.

Liu, K., Ostadhassan, M., 2017. Multi-scale fractal analysis of pores in shale rocks. J. Appl. Geophys. 140, 1–10.

Liu, K., Ostadhassan, M., Sun, L., Zou, J., Yuan, Y., Gentzis, T., Zhang, Y., Carvajal-Ortiz, H., Rezaee, R., 2019b. A comprehensive pore structure study of the Bakken Shale with SANS, N2 adsorption and mercury intrusion. Fuel 245, 274–285.

Li, W., Zhou, L., Liu, Y., Liang, S., Long, D., 1997. Evolution of sedimentary framework and environment of Turpan-Hami Basin. XJPG 18 (2), 135–141.

Li, W.H., 1997. Sequence stratigraphy of jurassic in Taibei sag, turpan-Hami Basin. Oil Gas Geol. 18 (3), 210–215.

Liu, X., Xiong, J., Liang, L., 2015. Investigation of pore structure and fractal characteristics of organic-rich Yanchang formation shale in central China by nitrogen adsorption/desorption analysis. J. Nat. Gas Sci. Eng. 22 (7), 62–72.

Loucks, R.G., Reed, R.M., Ruppel, S.C., Hammes, U., 2012. Spectrum of pore types and networks in mudrocks and a descriptive classification for matrix-related mudrock pores. AAPG Bull. 96, 1071–1098.

Mount, J.F., 1984. Mixing of siliciclastic and carbonate sediments in shallow shelf environments. Geology 12, 432–435.

Opera, Ali, Alizadeh, Bahram, Sarafdokht, Hashem, Janbaz, Mohadeseh, Fouladvand, Razieh, Mohamad Hosein Heidarifard, 2013. Burial history reconstruction and thermal maturity modeling for the middle cretaceous–early miocene petroleum System, southern Dezful Embayment, SW Iran. Int. J. Coal Geol. 120, 1–14.

Peters, K.E., 1986. Guidelines for evaluating petroleum source rock using programmed pyrolysis. AAPG (Am. Assoc. Pet. Geol.) Bull. 70 (3), 318–329.

Peters, K.E., Walters, C.W., Moldowan, J.M., 2005. The Biomarker Guide. Cambridge University Press, Cambridge.

Pfeifer, P., Ismail, I.M.K., 1994. Fractal analysis and surface roughness of nonporous carbon fibers and carbon blacks. Langmuir 10, 1532–1538.

Pour, A.S., Li, W.F., 2016. Fractal dimensions of shale. J. Nat. Gas Sci. Eng. 30, 578–582.

Saif, T., Lin, Q., Bijeljic, B., Blunt, M.J., 2017. Microstructural imaging and characterization of oil shale before and after pyrolysis. Fuel 197, 562–574.

Shao, X., Pang, X., Jiang, F., Li, L., Huyan, Y., Zheng, D., 2017. Reservoir characterization of tight sandstones using nuclear magnetic resonance and incremental pressure mercury injection experiments: implication for tight sand gas reservoir quality. Energy Fuel. 31, 10420–10431.

Sing, K.S., 1985. Reporting physisorption data for gas/solid systems with special reference to the determination of surface area and porosity. Pure Appl. Chem. 57 (4), 603–619.

Sun, Y., Guo, S., 2016. Qualitative and quantitative characterization of shale microscopic pore characteristics based on image analysis technology. Adv. Earth Sci. 31, 751–763.

Testamanti, M.N., Rezaee, R., 2017. Determination of NMR T 2 cut-off for clay bound water in shales: a case study of Carynginia Formation, Perth Basin, Western Australia. J. Petrol. Sci. Eng. 149, 497–503.

Tcherepanov, E.N., Droxler, A.W., Lapointe, P., Philippe, D.G., Bentley, S.M., Beaufort, L. P., Larry, C., Daniell, J., Opdyke, B.N., 2008. Neogene evolution of the mixed carbonate-siliciclastic system in the Gulf of Papua, Papua New Guinea. Journal of Geophysical Research Atmospheres 113 (F1), F01S21.

Waples, Douglas M., Kamata, Hiromi, Masahiro, Suizu, 1992. The art of maturity modeling, part 1: finding a satisfactory geologic model. AAPG (Am. Assoc. Pet. Geol.) Bull. 76 (1), 31–46.

Wang, M., Xue, H., Tian, S., Wilkins, R.W.T., Wang, Z., 2015. Fractal characteristics of upper cretaceous lacustrine shale from the Songliao Basin, NE China. Mar. Petrol. Geol. 67, 144–153.

Wang, S., Zou, C., Dong, D., Wang, Y., Huang, J., Guo, Z., 2014. Biogenic silica of organic-rich shale in Sichuan Basin and its significance for shale gas. Acta Sci. Nat. Univ. Pekin. 50, 476–486.

Wang, X., Zhang, L., Lei, Yu, Y., Jiang, C., Luo, X., Gao, C., Yin, J., Cheng, M., 2018. Characterisitics of migrated solid organic matters and organic pores in low maturity lacustrine shale: a case study of shale in Chang 7 oil-bearing formation of Yanchang Formation, southeastern Ordos Basin. Acta Pet. Sin. 39, 141–151.

Xiao, D., Yang, Z., 2013. Controlling factors and accumulation model of hydrocarbon accumulation in western Taibei Sag, Turpan-Hami Basin. J. Cent. S. Univ. 44, 679–686.

Xu, Q., Ma, Y., Liu, B., Song, X., Su, J., Chen, Z., 2019. Characteristics and control mechanism of nanoscale pores in lacustrine tight carbonates: examples from the Jurassic Da'anzhai Member in the central Sichuan Basin, China. J. Asian Earth Sci. 178, 156–172, 2019.

Xu, W., Du, X., Huang, H., Song, Z., Li, Z., 2019. Research Advances and Critical Issues of "mixed siliciclastic and carbonate sediments". Acta Sedimentol. Sin. 37 (2), 225–238.

Yang, C., Zhang, J.C., Tang, X., Ding, J.H., Zhao, Q.R., Dang, W., Chen, H.Y., Su, Y., Li, B. W., Lu, D.F., 2017a. Comparative study on micro-pore structure of marine, terrestrial, and transitional shales in key areas, China. Int. J. Coal Geol. 171, 76–92.

Yang, F., Ning, Z.F., Liu, H.Q., 2014. Fractal characteristics of shales from a shale gas reservoir in the Sichuan Basin, China. Fuel 115, 378–384.

Yang, R., He, S., Yi, J.S., Hu, Q.H., 2017b. Nano-scale pore structure and fractal dimension of organic-rich Wufeng-Longmaxi shale from Jiaoshiba area, Sichuan Basin: investigations using FE-SEM, gas adsorption and helium pycnometry. Mar. Petrol. Geol. 70, 27–45.

Yao, Y., Liu, D., Tang, D., Tang, S., Huang, W., 2008. Fractal characterization of adsorption-pores of coals from North China: an investigation on CH4 adsorption capacity of coals. Int. J. Coal Geol. 73, 27–42.

Ye, M., Xie, X., Xu, C., Du, X., Song, Z., Du, X., 2018. Discussion for classification—designation system of mixed siliciclastic-carbonate sediments and the implication for their reservoir prediction—A case study of mixed sediments from Bohai sea area. Geol. Rev. 64 (5), 1118–1131.

Zhang, S., Cao, Y., Zhu, R., Xi, K., Wang, J., Zhu, N., Hu, R., 2018. Characterization of lacustrine mixed fine-grained sedimentary rocks using coupled chemostratigraphic-petrographic analysis: a case study from a tight oil reservoir in the Jimusar Sag, Junggar Basin. Mar. Petrol. Geol. 99, 453–472.

Zhu, R., Zou, C., Wu, S., Yang, Z., Mao, Z., Yang, H., Fan, C., Hui, X., Cui, J., Su, L., Wang, H., 2019a. Mechanism for generation and accumulation of continental tight oil in China. Oil Gas Geol. 40, 1168–1184.

Zhu, X., Cai, J., Liu, Q., Li, Z., Zhang, X., 2019b. Thresholds of petroleum content and pore diameter for petroleum mobility in shale. AAPG BULLTIN 103, 605–617.

Zhu, Y.X., Li, X.N., Pu, Z.S., Zhao, H., Ma, Q., Song, X., 2014. The Qiketai tight oil reservoir characteristics of jurassic in Tuha basin. Xinjing Pet. Geol. 35 (2), 169–171.

Zou, C., Zhu, R., Bai, B., Yang, Z., Hou, L., Zha, M., Fu, J., Liu, K., Cao, H., Yuan, X., Tao, S., Tang, X., Wang, L., Li, T., 2015. Significance, geologic characteristics, resource potentialand future challenges of tight oil and shale oil. Bull. China Soc. Mineral Petrol. Geochem. 34, 3–17.